Study of neutrino signal from astronomical object in Super-Kamiokande

2019, March

Chenyuan Xu

Graduate School of
Natural Science and Technology
(Doctor's Course)
OKAYAMA UNIVERSITY

Abstract

This thesis focus on the study of neutrino signal search in Super-Kamiokande(SK), the largest water Cherenkov detector in the world. This thesis includes two topics: one is the coincident neutrino search in SK with the first detected gravitational wave produced by a binary neutron star merger, GW170817; another is the study of the de-excitation gamma signal from Charged Current Quasi-Elastic(CCQE) interaction of atmospheric neutrino in SK.

For the first topic, we searched for coincident neutrino events in the range from 4 MeV to 100 PeV, in a time window of ±500 seconds around the gravitational wave detection time, as well as during a 14 day period after the detection. No significant neutrino signal was observed for either time window. The upper limits on the neutrino fluence for GW170817 were calculated at 90% confidence level. From the upward-going-muon events in the energy region from 1.6 GeV to 100 PeV, the neutrino fluence limit is $16.0^{+0.7}_{-0.6}(21.3^{+1.1}_{-0.8})cm^2$ for $\nu_\mu(\bar{\nu}_\mu)$, with an error range of $\pm 5^\circ$ around the zenith angle of the source of GW170817, and the energy spectrum assumed as an index of -2. The fluence limit for neutrino energies less than 100 MeV, for which the emission mechanism would be different than for higher-energy neutrinos, is also calculated. The best limit is for anti-electron neutrinos under the assumption of a Fermi-Dirac spectrum with average energy of 20 MeV.

The second topic focus on an analysis method to directly measure the branching ratio of de-excitation gamma in CCQE interaction of atmospheric muon neutrino on Oxygen nucleus in water Cherenkov detector. The branching ratio of de-excitation gamma has not been directly measured yet, which causes not only the unreducable background component in Supernova Relic Neutrino search but also the systematic error in long baseline neutrino experiment. In this thesis, details about the method will be introduced, and the result of the direct search for de-excitation gamma in SK-IV real data will also be shown.

Acknowledgement

First of all, I would like to express my sincere gratitude to my supervisor Prof. Y. Koshio for giving me the opportunity to studying neutrino physics at Super-Kamiokande. This thesis would never exist without his kind support and excellent guidance.

I would like to appreciate Prof. M. Nakahata for giving me the opportunity to participate in the Super-Kamiokande experiment.

I would like to extend my gratitude to Prof. Y. Takeuchi, Dr. M. Smy, Prof. H. Sekiya, Prof. M. Vagins, Prof. L. Labarga, Prof. K. Okumura, Dr. L. Marti, Dr. M. Ikeda, Dr. T. Yano, Dr. E. O'Sullivan, Dr. Y. Nakajima, Dr. G. Pronost, Dr. P. Weatherly, Dr. S. Cao. They gave me great help and useful advice when I was working in LOWE and EGADS group.

I would like to appreciate Prof. M. Sakuda and Prof. H. Ishino, for their kind guidance in the physics leature in Okayama University.

I would like to appreciate Prof. J. Beacom, who support me a lot in both life and research when I was in Ohio State University.

I would like to thank to laboratory members or friends in Okayama University, Dr. S. Ito, D. Fukuda, K. Hagiwara, M. Harada, A. Hourai, H. Nagata, T. Hirashige, T. Kayano, Y. Wang, T. Mori, who gave me great help and support in my 5 years' life of PhD course.

Finally, I would like to express my greatest appreciation and gratitude to my family, relatives, and all my other friends.

Contents

1 Physics Background

1.1 Neutrino signal in Super-Kamiokande

Super-Kamiokande(SK) is a water Cherenkov detector. The purpose of Super-Kamiokande is various neutrino physics and the measurement of nucleon life time. It observed solar neutrinos [1], atmospheric neutrinos [49] as well as accelerator neutrinos [50], and several evidences for neutrino oscillations have been found. SK has been collecting data for more than twenty years and it is still the water Cherenkov detector with best sensitivity for MeV and GeV neutrino in the world.

This thesis is focused on two research topics. One is the coincident neutrino search in SK with the first detected gravitational wave produced by a binary neutron star merger, GW170817; another is the study of the de-excitation gamma signal from Charged Current Quasi-Elastic(CCQE) interaction of atmospheric neutrino in SK.

For the first topic, the mechanism of neutrino emission from binary star merger will be presented in this section. Especially for this research, two kinds of event reduction method are used for neutrino signal search below 100MeV: supernova relic neutrino search method and solar neutrino search method. In order to explain the purpose of the two, the related physics background will also be briefly introduced in this section, and the details about reduction steps will be in Section 6.

For the second topic, the essential purpose for this research is to estimate a kind of unreducable background in supernova relic neutrino search. This kind of background results from the atmospheric neutrino, and it not only be the most difficulty in current search but also remains unreducable in the next phase of SK. The motivation will be explained in this section, while the research plan, analysis status and current result will be shown in Section 8.

1.2 Binary Neutron Star merger

1.2.1 Neutrino Emission

On August 17th 2017 at 12:41:04 UTC, the Advanced LIGO and Advanced Virgo experiment identified the first evident signal of a gravitational wave from the binary neutron star merger, named GW170817 [2]. The interpretation is a merger of two compact objects consistent with neutron stars having total system mass of 2.74 solar masses and a luminosity distance of 40 Mpc.

The discovery of GW170817 marked not only a starting point of gravitional wave astronomy with binary neutron-star mergers, but also the possibility of multimessenger observation which can lead us to study the equation of state of supranuclear density matter [2]. Different to the gravitational wave events from binary black hole merger(such as the first detected gravitational wave event GW150914 [40]), the one from binary neutron star merger can enable the signal detection in electromagnetic channels [41]. In fact, associated observation of short gamma ray busrt GRB170817 as well as the brightening X-Ray emission are already been suggested [1, 42].

Since the high-density material reaches several tens of MeV via the binary neutron star merger, thermal neutrino emission could be expected from the remnant [7], unless the possibility that the remnant finally result into a black hole with prompt collapse, but fortunatelly this is not likely to happen when the maximum mass of spherical neutron stars exceeding $\sim 2M_{\odot}$ [43].

Direct detections of thermal neutrinos could be an important step in multimessenger astronomy, as the theoretical models of supernova explosions have been qualitatively confirmed by the detection of neutrinos from SN1987A [44]. However, little has been known about the realistic spectrum of neutrinos from binary neutron-star mergers so far. Monte-Carlo neutrino-transport simulations suggest that the spectrum can be approximated by pinched Fermi-Dirac distribution for as the case of supernova explosions [45].

The mechanism of neutrino emission from binary neutron star can be considered to follow these steps:

1. As the matter temperature getting high after the merger, pairs of e^- and e^+ are produced from thermal photons.

2. e^- and e^+ are captured on nucleons, from which ν_e and $\overline{\nu}_e$ are emitted with a rise time of $\sim 10ms$ Fig 1.

$$e^- + p \to \nu_e + n \tag{1}$$

$$e^+ + n \to \overline{\nu}_e + p \tag{2}$$

   In the case of binary neutron star merger, obviously the number of neutron is much higher than proton in neutron star, thus $\overline{\nu}_e$ is emitted much more than ν_e.

3. All neutrino type are made from e^-e^+ annihillation as:

$$e^+ + e^- \to \nu_x + \overline{\nu}_x \tag{3}$$

The peak luminosity of electron antineutrinos reaches $1 \sim 3 \times 10^{53} ergs^{-1}$ with the typical energy of $10 \sim 30$MeV depending on binary parameters and unknown equations of state for supranuclear-density matter.

1.2.2 Expected Neutrino Number in Detector

In Super-Kamiokande, the water Cherenkov detector with best sensitivity in the world for neutrino signals from MeV to GeV, the most dominating reaction in the expected energy range($10 \sim 30$MeV for neutrino from binary neutron star merger) is inverse beta decay(IBD) of electron antineutrino $\overline{\nu}_e(p+\overline{\nu}_e \to n+e^+)$.

The expected number of observed neutrinos for a single merger can be simply estimated as:

$$N_\nu = N_T \int_{t_i}^{t_f} \int_{E_{min}}^{E_{max}} \phi(E,t)\sigma(E)dEdt \tag{4}$$

Here N_T is number of protons, which is the target for IBD in water Cherenkov detector. $\phi(E,t)$ is the flux of $\overline{\nu}_e$ in unit energy. $\sigma(E)$ is the cross section of IBD for a $\overline{\nu}_e$ on a proton. t_i and t_f mean the starting and ending for time integral, while E_{min} and E_{max} represent the integral energy range.

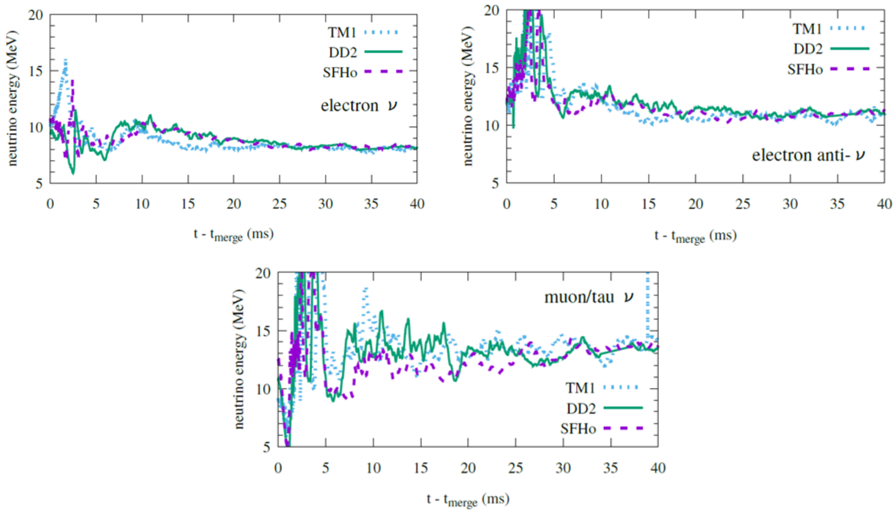

Figure 1: The expected neutrino energy after binary neutron star merger [8].

Considering the Fermi-Dirac distribution with temperature T, the average energy of neutrinos is $\langle E\rangle \approx 3.15k_BT$, while k_BT is Boltzmann constant. Ignoring time evolution, $\phi(E,t)$ can be given by:

$$\phi(E) = \frac{c}{2\pi^2(\hbar c)^3}\frac{E^2}{exp[E/k_BT]+1} \tag{5}$$

Where $\hbar$ is the reduced Planck constant. By taking the leading-order cross section from [46]:

$$\sigma_{LO}(E) = 9.5\times 10^{-42}cm^2(\frac{E}{10MeV})^2 \tag{6}$$

Equation 4 can be approximately written into:

$$N_\nu \approx 1.0\times 10^{-3}\times f_Ef_{SE}f_{OSC}(\frac{M_T}{1Mt})(\frac{E_{\Delta T}}{3\times 10^{52}erg})\times(\frac{\langle E\rangle}{10MeV})(\frac{D}{100Mpc})^{-2} \tag{7}$$

where M_T is detector volume and D is the distance from the source to the earth. In Equation 7, time integral is removed and the total energy of $\overline{\nu}_e$ emitted during $\Delta t_{obs}\approx 1s$ as $E_{\Delta t} = \int L_\nu d_t$ (L_ν is the Luminosity of $\overline{\nu}_e$), which is $\sim 3\times 10^{52}erg$ [47]. One reason for this is that the time evolution of luminosity has not been well understood, especially when $\Delta t_{obs} > 1s$.

The other three parameters in Equation 7 is f_E, f_{SE} and f_{OSC}. They respectively represent for the factor of the fraction of energy range, detection efficiency and the neutrino oscillation effect. Considering a integral range of $10\sim 50$MeV, f_E is 0.77 for typical energy $\langle E\rangle = 10MeV$ [8]. And in order to make an order estimation for neutrino events in Super-Kamiokande, here we ignore f_{SE} and f_{OSC} (the detection efficiency will be discussed in later section). Considering the fiducial volume 22.5kton of Super-Kamiokande and the luminosity distance of 40 Mpc, the expected order of neutrino events is $\sim 10^{-4}$, while siginificant signal could be detectable when the source is in a distance of $\sim 100kpc$. The result of neutrino signal search carried out in Super-Kamiokande will be introduced in later section.

1.3 Solar Neutrino

The Standard Solar Model (SSM) is the well-established theoretical model which has been constructed to explain the stellar evolution of the Sun [51]. In the core of the sun, the origin of the energy is from the the fusion of four protons into a ^4He as:

$$4p \rightarrow \alpha + 2e^- + 2\nu_e + 26.73MeV \tag{8}$$

Actually, reaction 8 is realized by two process: one is pp-chain; the other one is Carbon-Nitrogen-Oxygen (CNO) cycle. According to SSM, 98.4% of the total solar luminosity is produced by pp-chain process while the rest 1.6% is produced by CNO cycle.

The pp-chain includes reactions of:

$$p + p \rightarrow^2 H + e^+ + \nu_e \quad (\leq 0.420MeV, pp) \tag{9}$$

$$p + e^- + p \rightarrow^2 H + \nu_e \quad (1.442MeV, pep) \tag{10}$$

$$^7Be + e^- \rightarrow^7 Li + \nu_e \quad (0.861MeV(90\%), 0.383MeV(10\%),^7 Be) \tag{11}$$

$$^8B \rightarrow^8 Be^* + e^+ + \nu_e \quad (\leq 14.06MeV,^8 B) \tag{12}$$

$$^3He + p \rightarrow \alpha + e^+ + \nu_e \quad (\leq 18.77MeV, hep) \tag{13}$$

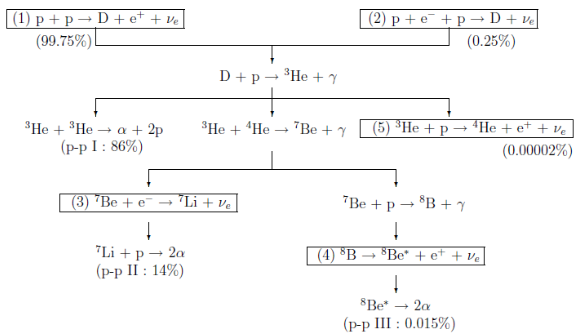

Figure 2: The pp-chain reactions

While CNO cycle include the reactions of:

$$^{13}N \rightarrow^{13} C + e^+ + \nu_e \quad (\leq 1.27MeV) \tag{14}$$

$$^{15}O \rightarrow^{15} N + e^+ + \nu_e \quad (\leq 1.73MeV) \tag{15}$$

$$^{17}F \rightarrow^{17} O + e^+ + \nu_e \quad (\leq 1.74MeV) \tag{16}$$

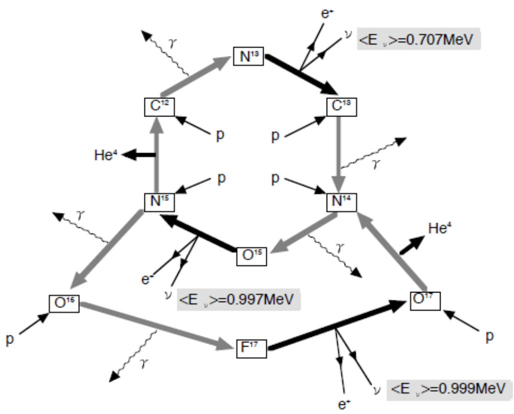

Figure 3: The CNO cycle reactions

The energy spectrum of different kinds of solar neutrinos predicted by SSM BP05(OP) [52](a revised version of SSM) is shown in Fig 4. The electron neutrino from the three reactions in CNO cycle, and *pp*, *pep*, ^7Be in pp-chain are with energy lower than the detection threshold of SK. Thus the detectable ones are ^8B and *hep*. Since *hep* flux is too low, the observation of ^8B spectrum becomes the most reliable way to study SSM.

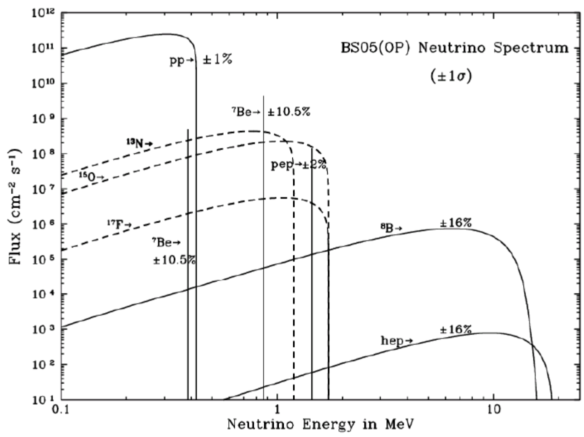

Figure 4: The solar neutrino energy spectrum predicted by the BP05 (OP).

1.4 Supernova Neutrino and Supernova Relic Neutrino

1.4.1 Supernova Explosion

On February 23rd 1987, supernova burst of Large Magellanic Cloud was observed. It is a supernova from about 51.4kpc distance from the earth and it is numbered with SN1987A. It is the first time that human detected the supernova by neutrinos and that is the sign of the birth of "Neutrino Astronomy". In SN 1987A, the neutrino detector KamiokaNDE observed 11 neutrinos [44], while American detector IBM observed 8 neutrinos [53]. The detection of supernova neutrino is not only a new page in the physics history but also proved that the fundamental model of core collapse supernova is correct. Study about supernova was based on optical observation in the past and it is limited by a lot of reasons. Neutrino has offered a new way to approach to the the mechanism of supernova explosion and cosmic evolution. Now experiments of supernova neutrino search are being carried out in the world wide.

To explain the mechanism of supernova explosion, the process can be divided as follows.

Beginning of core collapse

When the mass of the core exceed the Chandrasekhar Limit, the gravitational collapse will start and the density of the core will get larger and larger. ν_e will be released by electron capture(2) by the nuclei and the photodisintegration of iron nuclei(3) also occurs in this step.

$$e^- + A(N, Z) \to \nu_e + A(N+1, Z-1) \tag{17}$$

$$\gamma +^{56} Fe \to 13\alpha + 4n - 124.4MeV \tag{18}$$

Both of the two interactions will reduce the degenerate pressure and become the trigger of a rapid core collapse.

Neutrino trapping

When the density of the core exceeds $3 \times 10^9 g/cm^3$, the neutrinos will follows the coherent scattering(4) with the nuclei and be unable to go outside. This is called "neutrino trapping" and the boundary is called "neutrino sphere".

$$\nu + A(N, Z) \to \nu + A(N, Z) \tag{19}$$

Core bounce

When core density continue to increase and finally reaches the level of nuclear density($\sim 10^{14} g/cm^3$), the shock wave will be repulsed and driven towards outside.

Neutrino cooling

After the shock wave passed through, the matter outside the core will drop to the center and $\sim 10^{53}$erg of gravitational energy will be converted into thermal energy. All flavors of neutrinos will be produced by pair annihilation 20 and bremsstrahlung 21.

$$e^- + e^+ \to \nu + \bar{\nu} \tag{20}$$

$$N + N \to N + N + \nu + \bar{\nu} \tag{21}$$

$\bar{\nu}_e$ and ν_e will also be produce by electron capture 22 and positron capture 23.

$$e^- + p \to \nu_e + n \tag{22}$$

$$e^+ + n \to \bar{\nu}_e + p \tag{23}$$

Most of the energy are released by neutrinos and the star cools down in about 10s.

Supernova burst
The shock wave may takes several hours until it arrives the surface of the star. The penumbra part will be blasted off and the remnant of the star will become neutron star. Or if the mass of the core is heavy enough, it will finally become a black hole.

Summarizing this session, only ν_e can be emitted in the very beginning of supernova explosion, and later after that neutrinos of all flavors will be produced.

1.4.2 Supernova Relic Neutrino

As 99% of the energy is released by neutrino flux in supernova process, it is an important way to study supernova models by neutrinos. In Milky Way, core collapse supernova is estimated to be 2 or 3 times per century [54], and SK would observe $\sim 10^4$ events at a typical distance of 10kpc. From a supernova in the nearest galaxy Andromeda, SK would detect ∼1 event [29]. Although there is no supernova neutrino detected since SN1987A, all of the supernova exploded through the history of the universe have released neutrinos, and they are refered as Supernova Relic Neutrino(SRN) or Diffuse Supernova Neutrino Background(DSNB). The SRN spectrum is a convolution of a single supernova spectrum, by considering the supernova rate as a function of z, and neutrino energy redshifted. The first models for SRN were founded even before SN1987A [55], while the studies about SRN largely increased after SN1987A. Figure 2 shows the $\bar{\nu}_e$ fluxes predicted by the following theoretical models:

Constant SN rate model [56] (Totani et al. 1995)
The supernova rate was assumed as a constant in the whole universe in this model.

Population synthesis [57] (Totani et al. 1996)
It is founded by the same author by using a population synthesis of the stars in the galaxy evolution.

Cosmic gas infall model [58] (Malaney et al. 1997)
This model uses the supernova rate which is obtained from the density distribution of interstellar gas as a function of red shift parameter.

Chemical evolution model [59] (Hartmann et al. 1997)
This model considered the history of the cosmic star formation which is obtained from the chemical evolution.

Heavy metal model [60] (Kaplinghat et al. 2000)
In this model, the theoretical upper limit of SRN flux is predicted by using the abundance of heavy elements.

LMA neutrino oscillation [61] (Ando et al. 2002)
The parameter for neutrino oscillasion is considered in this model.

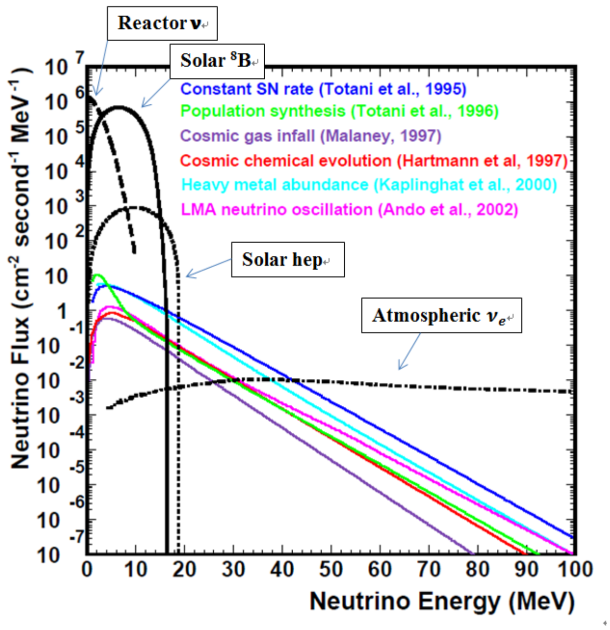

Figure 5: Colour lines are the $\bar{\nu}_e$ flux predicted by each model. Black lines represent other background neutrinos.

The reason why only $\bar{\nu}_e$ is considered is that the cross section of $\bar{\nu}_e$ reaction in water Cherenkov detector is two orders larger than the others in the main energy range of SRN. Even though $\bar{\nu}_e$ reaction has large cross section, SRN flux is still hidden in various background and has not been detected yet. As can been seen from the Figure 2, Solar and reactor neutrinos are dominant below 10MeV, and atmospheric neutrinos become dominant above 30MeV.

1.5 Quasi-Elastic neutrino reaction and de-excitation gamma

In water Cherenkov Detector, there are two kind of processes which can produce gamma. One is inelastic scattering $\nu +^{16} O \rightarrow \nu +^{16} O^*$, by which the excited Oxygen nucleus emit a nucleon or gamma rays between 1∼10 MeV. Another is quasielastic scattering, where nucleon is knock out from the Oxygen nucleus. Neutral Current Quasi-Elastic Scattering(NCQE) 24 and Charged Current Quasi-Elastic Scattering(CCQE) 25 both have de-excitation process, but through CCQE a muon will be produced. Calculation result shows that QE process overwhelms the inelastic process at neutrino energy of E_v >200MeV [15].

$$\begin{cases} \nu +^{16} O \rightarrow \nu + p +^{15} N^* \\ \nu +^{16} O \rightarrow \nu + n +^{15} O^* \end{cases} \tag{24}$$

$$\begin{cases} \nu_e +^{16} O \rightarrow e^- + p +^{15} O^* \\ \overline{\nu}_e +^{16} O \rightarrow e^+ + n +^{15} N^* \\ \nu_\mu +^{16} O \rightarrow \mu^- + p +^{15} O^* \\ \overline{\nu}_\mu +^{16} O \rightarrow \mu^+ + n +^{15} N^* \end{cases} \tag{25}$$

The CCQE signal from atomospheric neutrino is a kind of unreducable background for SRN search. Refering to the recent SRN analysis in SK [62], the sample has been applied with the coincident cut with a previous gamma or muon to remove atomospheric $\bar{\nu}_\mu$ CCQE events, but for those CCQE events with invisible muon and no de-excitation gamma, they still remains as the largest background in the final spectrum. Since the muon product can be invisible in SK, we hope to know the branching ratio of de-excitation gamma to estimate the remaining background component.

Oxygen has 8 protons and neutrons, 2 in $1p_{1/2}$ state, 4 in $1p_{3/2}$ state, and 2 in $1s_{1/2}$ state. Gamma can be released by de-excitation when $1p_{3/2}$ or $1s_{1/2}$ nucleon is knock out, for $1p_{1/2}$ case there is no gamma because it is already the ground state. Calculated result of the spectroscopic factors for each states is summarize in Table 1. Branching ratio for each state is from some indirect measurement, which uses electron or proton beam to make proton hole in Oxygen nucleus. These measurement has a constrain of proton observation, but since the energy level of proton and neutron is similar and ^{16}O is an isoscalr nucleus, we can roughly consider neutron case as the same.

NCQE cross section for on Oxygen was also measured by Tokai-to-Kamioka (T2K) long baseline oscillation experiment with a median neutrino energy of 630MeV, while in the result, de-excitation gamma was observed in SK and the NCQE and CC component was estimated from simulation [16].

Unlike NCQE, CCQE interaction gives a muon signal and a coincident search for decay electron can ensure the correctness of CCQE event selection. However, the difficulty is muon signal and de-excitation gamma appears from the same position and they occur in a time difference less than 1ns. The analysis method will be introduced in Section 8.

	$1p_{1/2}$	$1p_{3/2}$	$1s_{1/2}$
Spectroscopic Factor	0.632	0.703	0.422
$Br(\gamma > 6MeV)$ from p-hole	0%	91.8%	14.7%
$Br(\gamma > 6MeV)$ from n-hole	0%	86.9%	14.7%

Table 1: Spectroscopic factors and branching ratios for ^{16}O de-excitation γ ray above 6MeV. Spectroscopic factors are from calculated result [15], branching ratios are from measurement which make proton or neutron holes in ^{16}O by electron or proton beam [17–19].

2 Super-Kamiokande detector

2.1 Detector Structure

Super-Kamiokande (SK) is a water Cherenkov detector built for neutrino observation [20]. The last three letters can be explained as two meanings: "Neutrino Detection Experiment" and "Nucleon Decay Experiment". SK is located at latitude $36°25'N$ and longitude $137°18'E$, Mt.Ikenoyama of Gifu Prefecture, Japan. It is a water tank of cylinder shape, with 39.3m diameter and 41.4m height, filled with 5kton ultra water. SK is built in 1000m underground, where was once one of the world's largest Zinc mines but now used for neutrino detection experiment. Since the underground environment, SK avoid suffering from the high rate background of down-going cosmic muons. SK observe an average rate of cosmic muon by ~2Hz, which is 10^{-5} comparing with the mountain surface.

Additionally, SK has a structure of two layers to reject the muon backgrounds: An inner detector(ID) with 11139 (in SK-IV) inward-facing 20-inch Photomultiplier Tubes (PMT), and an outer detector(OD) with 1885 outward-facing 8-inch PMTs. The inner volume is 32.5kton, the PMT coverage is $\sim 40\%$ (except SKII) and the rest $\sim 40\%$ is covered by polyethylene black sheet to reduce the unneccessary photon reflection. The outer detector part is 2m thickness, also filled with water, and can be used as veto signal for cosmic rays as well as the gamma rays from the surrounding rock, because those signals will give Cherenkov light in the outer detector before they enter the inner part. Also, the wall of the rock in the mine is covered by "Mineguard", a polyurethane material which can prohibits the radon from the rock. The dome above the tank is used for 5 electronics huts, a linear accelerator used for detector calibration, and storage for various equipment. The data acquisition system will be explained in Section2.3, while the calibration methods will be in Section 5.

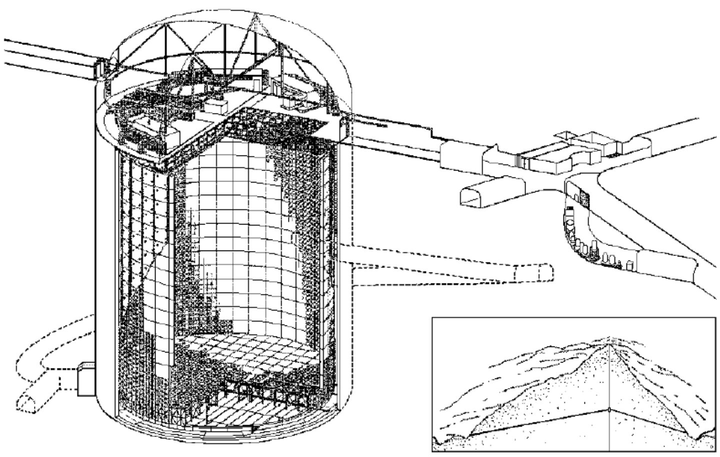

Figure 6: The detector appearance. The bottom right shows the location within the mountain. (cutaway view)

2.1.1 History and current status

SK has five stages(including the latest one), called SKI, SKII, SKIII, SKIV and SK-Gd. SK start running from April 1996 with 40% ID cathode coverage and 11146 ID PMTs, and stopped in July 2001 for routine maintanance and upgrades. The period from April 1996 to July 2001 is referred as SK-I period. During this period, in 1998, the SK collaboration released the first highly significant experimental evidence for neutrino oscillations as well as the solar deficit.

On November 12, 2001, after the maintenance was completed and the tank was being refilled with water, a catastrophic accident occurred. One of the PMTs imploded when the tank was ~75% full, causing a chain reaction resulting in the implosion of almost all the underwater PMTs. The chain reaction was violent enough that it registered as a seismological event to a seismological recorder 8.8 km distant. 6665 out of 11146 ID tubes were found to be destroyed. The water was drained again, and the broken glass cleaned. Unfortunately remaking so many PMTs is a time consuming process, and it was decided to run the detector in the meantime. The surviving tubes were redistributed throughout the detector, after being fitted with new acrylic coverings (tube front) and 'FRPs' (fiberglass reinforced plastic, tube back), to prevent the shock wave of any future tube implosions from causing another chain reaction. The detector was turned back on with 19% cathode coverage (47% that of SK-I), and ran until the new PMTs were ready in July 2005. This period of data is referred to as SK-II.

The refitting of the PMTs took almost a year, and the detector was operational again in June 2006. In August 2008, the SK electronics system was completely overhauled and a new upgraded system was put in place. The data period from June 2006 to August 2008 is called SK-III. Since September 2008, after the electronics upgrade was completed, data taking has continued, and this period is referred as SK-IV.

During SK-IV, a project proposed to disolve Gadolinum into SK tank has been planned [29]. Gadolinum can enable the detector to distingush neutrino and anti-neutrino, by making the neutron signal produced in anti-neutrino interaction to be visible. Various works have been carried out, such as Gadolinum quality check, impurity search, Gadolinum circulation system design and so on. In order to test Gadolinum performance, a 200ton water Cherenkov detector called Evaluating Gadolinium's Action on Detector System (EGADS) was built inside the same mine with SK. Since the success of EGADS experiment and the provement of feasibility of Gadolinum project, SK was shut down in May 2018 for Gadolinum disolving work. With Gadolinum-load detector, SK started a new stage from October 2018, called SK-Gd.

Overall, SK-IV is the most stable and long-lasting period of SK, and in this thesis, most of the analysis will be based on the data set of SK-IV.

2.2 Dection method

2.2.1 Cherenkov radiation

SK is a water Cherenkov detector, it detects the neutrino by observing Cherenkov light. The speed of light in medium is c/n, when the index of refraction is n. If a charged particle passes through the medium with velocity

Phase	SK-I	SK-II	SK-III	SK-IV	SK-Gd
Start	Apr 1996	Oct 2002	Jul 2006	Sep 2008	Nov 2018
End	Jul 2001	Oct 2005	Aug 2008	Jun 2018	Running
ID PMT	11146	5182	11129	11129	11129
OD PMT	1885	1885	1885	1885	1885
PMT Coverage	40%	19%	40%	40%	40%
Electronics	ATM	ATM	ATM	QBEE	QBEE
Energy Thre.	4.5MeV	6.5MeV	4.0MeV	3.5MeV	-

Table 2: The summary of characteristics of each SK phase. Energy threshold is the recoil electron kinetic energy, adopted for the analysis. The threshold of SK-Gd is not shown because currenly when this thesis is being written, SK-Gd is still in test.

larger than c/n, the particle will emit a forward cone of light. This is named as Cherenkov radiation, while P.A.Cherenkov is the person who discovered this effect in 1934. To theoretically explain it, when a charged particle travels in the medium, it will emit spherical wave by electric polarization. If the velocity of the particle exceeds c/n, the spherical waves can interfere with each other and form radiation. Otherwise, they will never meet each other and stay independent.

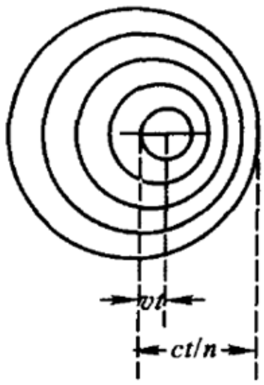

Figure 7: when velocity of the charged particle is smaller than c/n

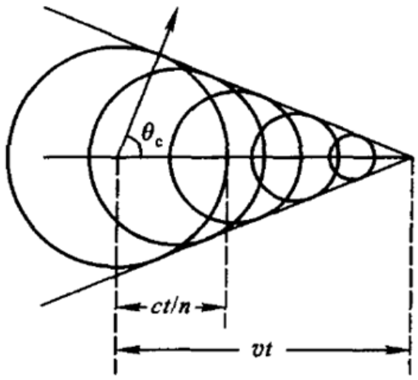

Figure 8: when velocity of the charged particle is larger than c/n

Thus, the angle θ between Cherenkov light and the direction of the charged particle can be calculated with the ratio of light velocity in the medium c/n and the velocity of incident particle as follows:

$$\cos\theta = \frac{1}{n\beta} \tag{26}$$

Here $\beta = v/c$. Considering the critical condition of Cherenkov radiation is $\beta \geqslant 1/n$,the energy threshold for incident particle to emit Cherenkov light is:

$$E_{thr} = \frac{nm}{\sqrt{n^2 - 1}} \tag{27}$$

Particle	Threshold(MeV)
$e^{\pm}$	0.767
$\mu^{\pm}$	157.4
$\pi^{\pm}$	207.9

Table 3: Cherenkov threshold for charged particles in water.

For water Cherenkov detector, the index of refraction is 1.33, so the threshold of total energy for the main particles is shown below.

In most cases, the signals observed in Super-K are from electrons or muons with $\beta \approx 1$, so the Cherenkov angle is close to 42°. The number of photon (N) produced by Cherenkov radiation in unit length dL can be calculated as:

$$\frac{d^2N}{d\lambda \mathrm{d}L} = \frac{2\pi\alpha Z^2}{\lambda^2}(1 - \frac{1}{n^2\beta^2}) \tag{28}$$

Here λ is the wavelength of Cerenkov radiation, Z is the charge of incident particle, and α is fine-structure constant. By integrating it, the number of photon in specific wavelength range (λ_1, λ_2) is:

$$\frac{dN}{dL} = \frac{2\pi\alpha Z^2}{n}(\frac{1}{\lambda_1} - \frac{1}{\lambda_2})(1 - \frac{1}{n^2\beta^2}) \tag{29}$$

For example, when an electron travels 1cm in Super-K tank with $\beta \approx 1$, about 340 photons would be produced in Super-K PMT sensitive range of 280nm∼660nm. It can hardly be observed and that is why we need photon-multiplier tubes (PMT).

To consider muons, they can be more complicated because of the continuous emission of light as the muon is usually energitic to travel through the tank. Some muons are created by neutrino interactions, but most of the muons are cosmic ray muons (∼2 Hz) which is able to penetrate the rock overburden and enter the detector. These events can be easily distinguished by use of the OD, and the entire muon track can usually be reconstructed. Other charged particles, such as pions, are also seen.

SK is capable to observe neutrinos from the sun, from atmospheric cosmic ray interactions, from supernovae, from neutrino beams, and most likely from nuclear reactors. Due to the large volume of SK, the detector is also useful for proton decay and dark matter searches.

2.2.2 Photomultiplier tube

The PMTs being used in Super-K are produced by Hamamatsu Photonics c.o, and the development work was done under the cooperation of Super-K group. The inner detector PMTs are 20-inch Hamamatsu R3600 PMTs, and the outer detector PMTs are 8-inch Hamamatsu R1408 PMTs [21]. The design of inner detector PMTs are based on the PMTs being used in KamiokaNDE experiment, with several improvements.

Figure 10 shows the structure of a PMT. The photocathode material is bialkali(Sb-K-Cs) which has a sensitive region of 300-600nm and the quantum efficiency peaks at 360-400nm as shown in Figure 12. Electron photons could be multiplied with a gain of $\sim 10^{\ 7}$ by 11 chain dynodes. A good time resolution

Photoelectronic Surface	50cm
Material	Sb-K-Cs
Dynode	Venetian Blind type
Quantum Efficiency	22% at 390nm
Dark Rate	3.5kHz
Time Resolution	3ns RMS at 1pe

Table 4: Properties of Super-K inner PMT

is critical to have better vertex resolution for low energy events. For single photoelectron the transit time spread is about 2.2 ns. The desired 1 p.e. peak can be clearly seen in Figure 13, where the peak close to zero ADC count is due to the dark current. Super-K PMTs not only have better time resolution than Kamiokannde PMTs, but also become able to identify single photon signals. It is an improvement of great significance because most of the signals in low energy events like supernova neutrinos are due to single photon.

Figure 9: Photo of a bare PMT

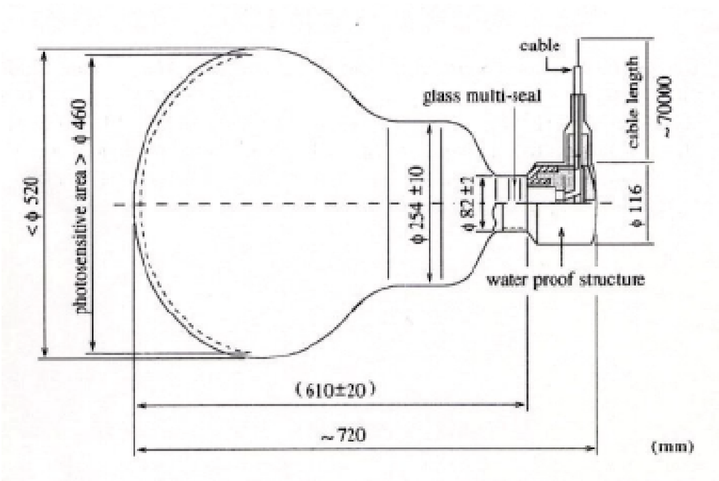

Figure 10: Inner structure of PMT

Figure 11: The acrylic cover and FRP case used from 2001 to protect the PMT from shock wave [20].

The threshold is set to 1/4 pe and the rate of dark noise above this threshold was ∼3.5 kHz when in Super-K first phase. The magnetic field of the earth can largely affect the photoelectrons so Helmholtz coils are used for compensation. The residual geo-magnetic field is kept less than 100 mG in every position of the tank.

In the accident happened in 2001, about half of the PMTs were broken as a result of shock wave. Since that, PMTs in Super-K are all installed with acrylic covers and FRP cases as shown in Figure 11. The transmittance of the acrylic cover is about 96% and it doesn't affect the event reconstruction.

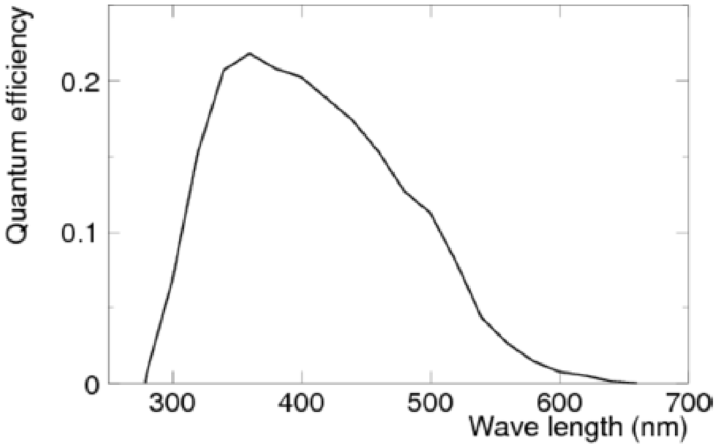

Figure 12: The quantum efficiency of 50cm PMT as a function of wavelenth.

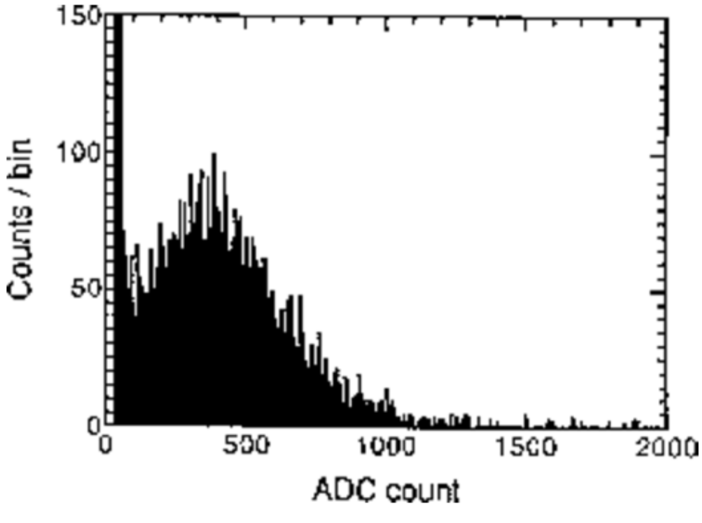

Figure 13: Single photoelectron pulse height distribution.

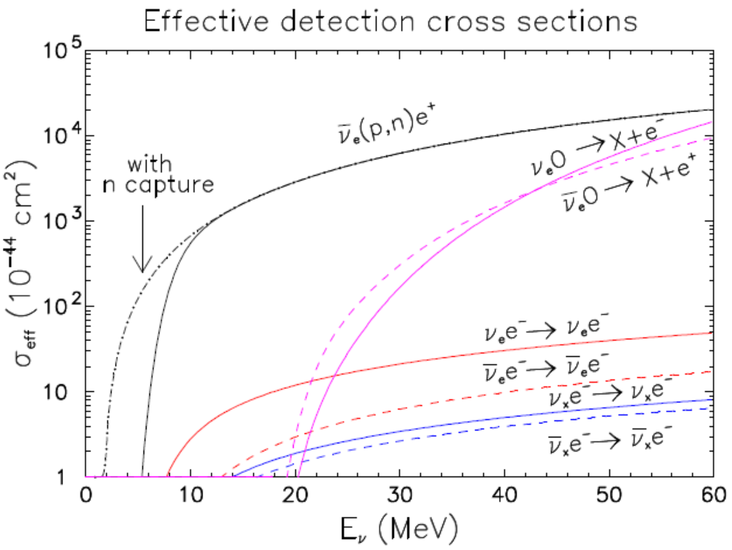

Figure 14: Neutrino interaction cross sections in a large water Cherenkov detector, including resolution and threshold effects [27].

2.2.3 Neutrino interaction in water Cerenkov detector

The neutrinos react with electrons or Oxygen in water and finally charged particles are observed by Cherenkov radiation. The main reactions of neutrinos in water Cerenkov detector is shown below.

Inverse Beta Decay:

$$\overline{\nu}_e + p \rightarrow n + e^+ \tag{30}$$

This is the most dominant interaction and it has the largest cross section in the energy region of Supernova neutrinos. It occurs between the anti-neutrinos of electron type and free protons in water. Most of supernova neutrinos will be detected via this interaction. However, the direction information will be lost in this interaction.

Neutral Current Interaction:

$$\nu_x + {}^{16}O \rightarrow \nu_x + \gamma + X \tag{31}$$

Elastic Scattering:

$$\nu + e^- \rightarrow \nu + e^- \tag{32}$$

This is the elastic scattering between neutrinos and electrons in water. It happens in all flavours, but the electron-neutrino has about 6 times larger cross section than others. This is main reaction for solar neutrino detection, as the solar neutrino only has ν_e. For supernova neutrino, the cross section of elastic scattering is two order smaller than inverse beta decay but it can conserve the direction information of the incident neutrinos, which is very important for the early announcement to the other measurement such as optical observation, gamma-ray and so on.

2.3 Data acquisition system

2.3.1 Electronics

There are 5 huts on the top of the SK tank, named with a "Central hut" and four "Electronics huts". In the electronics huts, HV power supplies and the electronics system are placed; the former supplies high voltage to ID and OD PMTs and the latter digitizes the analog signal from the PMTs. In the central hut, the trigger system and the control electronics are placed and the signals digitalized in the four Electronics huts are merged. Electronics of SK changed from SKIV. The difference is front-end part. From SKI to SKIII, the front-end electronics is called the Analog Timing Module (ATM) [23, 24], which is based on TKO (Tristan KEK Online) standards [25]. From SKIV, QTC-Based Electronics with Ethernet (QBEE) [25] is used. The most difference between ATM and QBEE is, in ATM period data is recorded with hardware trigger, while QBEE collect all the data and apply software trigger later.

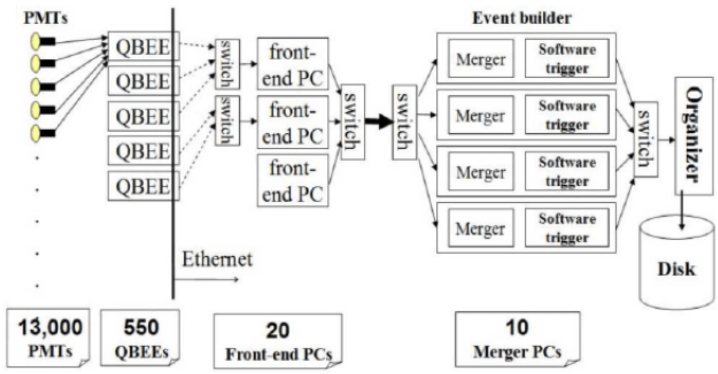

Figure 15: The schematic view of the DAQ system used in SK-IV [28].

2.3.2 Trigger

The detector has triggers for ID and OD. ID triggers includes 4 types: Super Low energy (SLE) trigger, Low energy (LE) trigger, High Energy (HE), Super High Energy (SHE). The four types of ID triggers are seperated by different HITSUM threshold.

The HE trigger is mostly used for atmospheric neutrino studies. The LE trigger is good for SN relic events and solar neutrino events. The SLE trigger was introduced to look for low energy solar neutrino events. The lower threshold of the SLE trigger causes a much higher trigger rate (roughly an order of magnitude more triggers per MeV the threshold is lowered). Much of the increase comes from background, such as gammas from the rock walls and radioactivity from

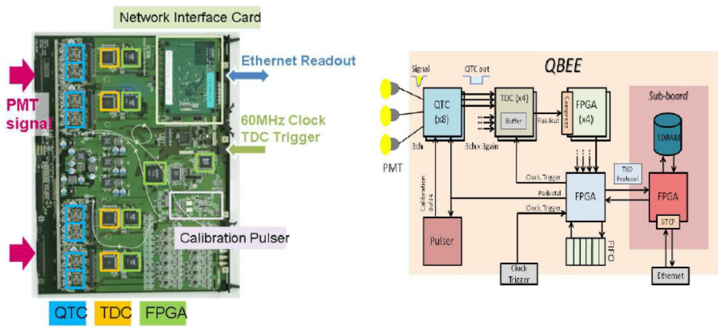

Figure 16: Left: The picture of the new front end electronics QBEE. Right: The block diagram of the signal processing in the QBEE.

the PMT glass itself. In order to effectively lower the low energy threshold and not be swamped by background, a prefilter was introduced for SLE events called the intelligent trigger (IT).

The IT does a quick vertex fit to SLE events and only saves those within the fiducial volume (inner 22.5 ktons), eliminating much of the background. As computing power increased throughout SK-I, the IT system was upgraded to handle a higher event rate, and the SLE threshold was lowered multiple times as SK-I progressed. During SK-II, all thresholds were lowered to reflect the decreased cathode coverage. Trigger thresholds are summarized in Table 2.1. The OD trigger has remained constant at 19 OD hits.

	SLE	LE	HE	SLE
Threshold (hit)	31	34	45	51
Gate width (μs)	-0.5$\sim$1.0	-5$\sim$40	-5$\sim$40	-5$\sim$40

Table 5: The threshold for each trigger and its event time width.

3 Event Reconstruction

3.1 low energy event

3.1.1 Vertex reconstruction

In SK analysis, usually the events below 100MeV are considered as low energy events, and those above 100MeV are considered as high energy events. For low energy events, the expected signals are the Cherenkov light of the electrons and positrons around 10MeV. Those electrons or positrons are most from neutrino-electron elastic scattering or inverse beta decay with proton. Since the energy loss of electron in water is ∼2MeV/cm, the travel distance before stopping in the tank is usually very short (∼10cm). As a result, for low energy event, the Cherenov light source can be considered as a point. Another fact is, in the low energy as ∼10MeV, most of the hit PMTs can only get one photon, thus the charge response of the PMTs become insignificant.

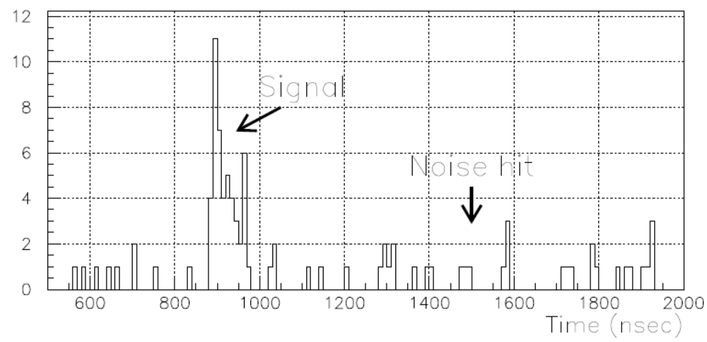

Figure 17: The timing distribution of hit-PMTs in one event. Horizontal axis is the relative timing of the each hit-PMT obtained from data.

There are several vertex reconstruction fitter in SK, Kai fit, Clus fit, and currently the one with best vertex resolution is called BONSAI (Branch Optimization Navigating Successive Annealing Interactions) fitter [35].

BONSAI search for the vertex by 2 steps :

1. Many possible starting points are constructed out of combinations of four hit PMTs. Then substract the time of flight for the photon from the test point $\vec{x}$ to each hit PMTs as $t - t_{tof} - t_0$, while t is the original time response from PMT, t_{tof} is the time of flight, and t_0 is the time offset. Figure 17 shows the time response of all the hit PMT in one typical event.

2. Calculate the likelihood for the test point $\vec{x}$. The likelihood is defined as:

$$\mathcal{L}(\vec{x}, t_0) = \sum_{i}^{N_{hit}} \log(P(t - t_{tof} - t_0)) \tag{33}$$

   $P(t - t_{tof} - t_0)$ is the probability density function (PDF) of the timing residual for a single photoelectron signal as shown in Figure 18. The PDF is made from LINAC calibration data (will be explained later).

3. Find the best point by maximizing the likelihood after checking against 12 nearby points on a grid of successively smaller sizes, which is down to 1 cm. The dark noise background is considered to be flat in time axis. The fitter also returns a fit goodness value which can be used to evaluate the quality of the fit and identify misfits.

$$g_v = \frac{\sum^{allhit} e^{-(\frac{t_t - tof(i) - t_0}{\sqrt{2}\omega})^2} e^{-(\frac{t_t - tof(i) - t_0}{\sqrt{2}\delta})^2}}{\sum^{allhit} e^{-(\frac{t_t - tof(i) - t_0}{\sqrt{2}\omega})^2}} \tag{34}$$

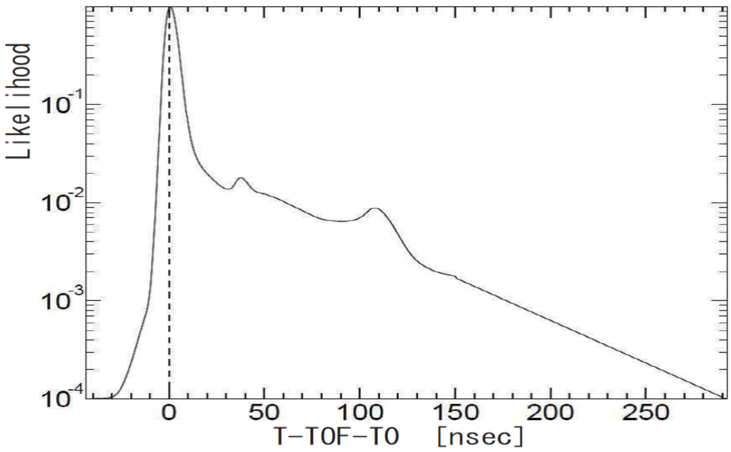

Figure 18: Timing PDF used for vertex reconstruction in BONSAI fitter. The PDF is made from LINAC calibration data. The peaks around 40nsec and 110nsec are caused by the after pulses.

3.1.2 Direction reconstruction

Sine the Cherenkov light makes a ring-like pattern of photons, it is possible to reconstruct the direction of the event. The direction reconstruction uses a maximum likelihood function which is defined as:

$$\mathcal{L}(\vec{a}) = \sum_{i}^{N_{20}} \log(f(cos\theta_i, E)) \times \frac{cos\Theta_i}{a(\Theta_i)} \tag{35}$$

1. N_{20}: The number of hit PMTs inside 20nsec window near $t - t_{tof} - t_0 = 0$
2. $f(cos\theta_i, E)$: θ_i is the angle between the particle direction and the vector from the vertex to i-th hit PMT. $f(cos\theta_i, E)$ is the expected PDF of θ_i, which depends on the energy because the particle with different energy will suffer from multiple Coulomb scattering at different degrees. The energy dependence is evaluated by SK simulation of mono-energetic electrons.

3. $\frac{cos\Theta_i}{a(\Theta_i)}$: Θ_i here means the angle between the verticle direction from i-th PMT surface and the vector from reconstructed vertex to i-th PMT, which means Θ_i is the expected incident angle. $a(\Theta_i)$ is the photon acceptance of i-th PMT, depending on the incident angle.

The directions are scanned by grid search, each direction is estimated and finally the best one will be selected as reconstructed direction. To explain more about the estimation method: firstly, the vertex and tentative direction are already known, a hit PMT(either is fine) is choosed as the starting point and the vector from vertex to starting point is used as a reference; secondly, for the other hits, the azimuth angle to the reference vector is caculated and then the azimuth angle distribution is made(example event shown in Fig 19); thirdly, the uniformity of the azimuth angle distribution is defined by the arrow length shown in Fig 19. If the event is normal, the distribution is uniform and the arrow length is small. On the other hand if the hits intend to be a cluster, then the arrow length is large.

After the recontructed direction is fixed, the recontruction precision is calculated by Equation 36, which means a Kolmogorov–Smirnov test between the real event and a ideal event with the same number of hits uniformly distributed on the Cherenkov cone.

$$g_d = \frac{max[\theta_{uniform}(i) - \theta_{data}(i)] - min[\theta_{uniform}(i) - \theta_{data}(i)]}{2\pi} \tag{36}$$

From the defination we could know that when $g_d = 0.0$ it means the best fit, and when $g_d = 1.0$ it means the most poor fit. g_d will be recorded as well as the reconstructed direction, to be used for background removing in later process.

3.2 Mu event

Muons in the detector were fitted by software tool called Muboy. Muboy is designed for a passing-through muon that it is searching for the entry position and exit position of the muon. However, it not only fits simple single through-going muons with a single entry and exit position, but actually looks for different types of muon events as it fits, and categorizes the event accordingly. Muboy categorize each event as being one of the following:

1. Single through-going($\sim 82\%$). This is the most common case. The muon simply entry the tank, and then goes out.

2. Stopping muons($\sim 7\%$). The muon stops inside the tank, which means it has an entry position but no exit position. Usually the muon will decay to electron after it stops.

3. Multiple tracks($\sim 7\%$). More than one track are found.

4. Corner clipper($\sim 7\%$). The muon with very short track length($L < 7m$). Usually it refers to the muons entry from the top and then exit from the barrel.

Muboy is not the only muon fitter in SK, but it is capable to categorize muon into different types and fit the multiple tracks. A fitting goodness is also

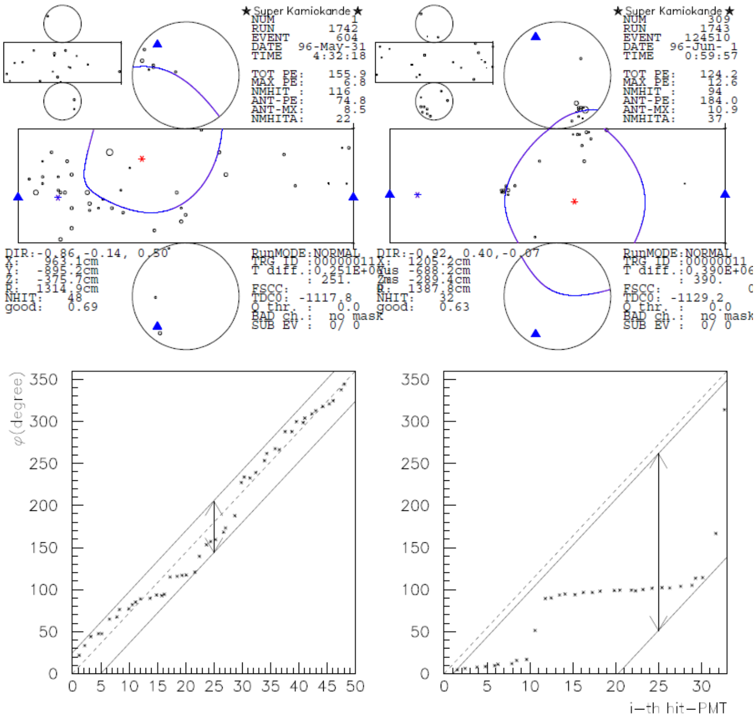

Figure 19: Left figure is shown as normal event and the right one is the event with small cluster. Lower distribution fill the azimuth angle of each hit-PMT from the start of one point [31].

given, while in case of multiple track, each track will have a fitting goodness. SK has other fitters which are also able to fit muon. One is APfit, currently the official reconstruction tool for high energy analysis. Another is fitQun, a newly developped recontruction tool with better precision, but have not been used as official yet. However, since this thesis is mainly about low energy analysis, the details about APfit or fitQun, as well as the fitting algorithm, will not be discussed.

4 Simulation

4.1 SKdetSIM overview

SKdetsim is the Monte Carlo(MC) simulation software of Super-K detector. It's based on Fortran language and GEANT3.21 simulation framework [39], which is developed by CERN, widely used in high energy experiments, and qualified by many physicists. Most of the physics process in SKdetsim follow GEANT3, except that the parts of Cherenkov photon generation and photon propagation in water are customized by SK group. This is because when SKdetsim was been developed, the GEANT3 version at that time didn't have the package for Cherenkov process.

The simulation process can be seperated into four steps to help to understand:

1. Particle generation.
2. Particle tracking and Cherenkov photon emission
3. Progration of Cherenkov photon
4. PMT response and electronics simulation

The four steps will be explained in the following subsections.

4.2 Particle generation

SKdetsim is used for different purposes: solar neutrino, supernova relic neutrino, high energy analysis, and calibration analysis. It should be mentioned that SKdetsim does not treat the neutrino reaction itself. For solar neutrino, the events are made by ^8B and hep flux at earth, then the cross section of neutrino reaction is taken into calculation and finally the recoil electrons are given into SKdetsim to simulate the signal in the tank. Simulation for relic neutrino does the similar thing, but the Ando LMA model and HBD 6 MeV model are used for neutrino source, and Strumia and Vissani's calculation for cross section of Inverse Beta Decay is used. For the simulation of LINAC calibration, the pipe is defined in SKdetsim program and the electron is generated from the pipe at fixed energy. For the simulation of Ni calibration, the Ni ball is defined but the gamma is generated by a pre-loaded spectrum, not from the ^{252}Cf source and Ni-neutron reaction as the real case.

However, this thesis does not focus on solar neutrino spectrum or relic neutrino spectrum, though the data set of those two are used later. So the detail of neutrino spectrum generation and cross section of neutrino reaction will not be discussed here.

4.3 Particle tracking and Cherenkov photon emission

When the particle is generated into tank water, SKdetsim track the particle by each small step. The dominant processes for low energy region(a few MeV to a few tens MeV) are multiple scattering, ionization loss, δ-ray production, bremsstrahlung and annihilation of positrons for electrons, pair creation, Compton scattering and photoelectric effect for gammas. In each step, SKdetsim calculate the flying distance, energy loss, direction change, and the physics process happened in this step. If there is any secondary particle(including Cherenkov photon) produced in this step, the information of the secondary particles will be saved into the buffer memory and be tracked later. Usually when a charged particle goes below the Cherenkov threshold, SKdetsim will stop the tracking.

In particle tracking, the other physics processes follow GEANT3 and detail information can be found in GENAT3 manual. Special attention should be paied to Cherenkov photon production, as this part is the exception that it is developed by SK group. For each tracking step, the Cherenkov photon number N is give by equation 37.

$$d^2N = \frac{2\pi\alpha}{n(\lambda)\lambda^2}(1 - \frac{1}{n^2\beta^2})dxd\lambda \tag{37}$$

Here the n is the refractive index of water($n \approx 1.33$), α is the fine structure constant, and β is the velocity of the electron in unit of the light velocity in vacuum. In per track length dx, dN is calculated on per wava length $d\lambda$. It should be mentioned that only the range of 300-700nm is intergrated because PMT is only sensitive to this region. The number of Cherenkov photon produced is approximately proportional to the energy of electron, this property is used to determine the energy scale as explained in previous section. The direction of Cherenkov photon is given by equation 38.

$$cos\theta = \frac{1}{n\beta} \tag{38}$$

θ here is the open angle.

4.4 Progration of Cherenkov photon

The velocity of Cherenkov photons depends on its wavelength. The group velocity can be evaluated as:

$$v_g = \frac{1}{n(\lambda - \lambda\frac{dn(\lambda)}{dn})} \tag{39}$$

where c is light velocity in vacuum, λ is light wavelength, was used for the light velocity in the water. The denominator of this equation can be treated as "effective index".

Though the refractive index of water is ~1.33, actually it depends on the wave length as:

$$n(\lambda) = \sqrt{\frac{a1}{\lambda^2 - \lambda_a^2} + a2 + a3\lambda^2 + a4\lambda^3 + a5\lambda^6} \tag{40}$$

The parameters are summarized below, and they are obtained from real measurements.

When the photon is reflected or scattered, the direction vector changed and the tracking will continue. While the photon is absorbed in water, it will be killed and the tracking will be stopped. The intensity of the light traveling in water exponentially decreases as:

$$I(x) = I_0(\lambda)exp(\frac{-x}{L(\lambda)}) \tag{41}$$

λ_a^2	0.018085μm
a_1	$5.7473534 \times 10^{-3}\mu m$
a_2	$1.769238\mu m$
a_3	$-2.797222\mu m$
a_4	$8.715348\mu m$
a_5	$-1.413942 \times 10^{-3}\mu m$

Table 6: 111

Here x is the traveling length, $L(\lambda)$ is the total attenuation length, $I_0(\lambda)$ is the initial light intensity. The total traveling consist of absorption, Rayleigh scattering and Mie scattering. The three coefficients in total attenuation can be understood as:

$$L_{attn.} = \frac{1}{\alpha_{abs}(\lambda) + \alpha_{Rayleigh}(\lambda) + \alpha_{Mie}(\lambda)} \tag{42}$$

From the measurement result, it is difficult to know the Mie scattering part from the total scattering. However one feature we know is that Rayleigh scattering is symmetric in forward and backward, while Mie scattering is asymmetric and it scatter more light to the forward direction. So the equation above can be modified to:

$$L_{attn.} = \frac{1}{\alpha_{abs}(\lambda) + \alpha_{sym}(\lambda) + \alpha_{asym}(\lambda)} \tag{43}$$

α_{sym} and α_{asym} are the sysmmetric and asysmmetric component in scattering respectively. α_{sym} consist of Rayleigh and symmetric Mie scattering, while α_{asym} consist of forward Mie scattering.

In SKdetsim, they are calculated as empirical function as:

$$\begin{cases} \alpha_{abs}(\lambda) = P_0 \times \frac{P_1}{\lambda^4} + C \\ \alpha_{sym}(\lambda) = \frac{P_4}{\lambda^4} \times (1.0 + \frac{P_5}{\lambda^2}) \\ \alpha_{asym}(\lambda) = P_6 \times (1.0 + \frac{P_7}{\lambda^4} \times (\lambda - P_8)^2) \end{cases} \tag{44}$$

$P_0 \sim P_8$ are fitting parameters tuned by calibration data, the parameter C in α_{abs} is the amplitude based on the experimental data.

4.5 PMT response and electronics simulation

When the photon arrive the PMT surface, it can be reflected or absorbed. When it is absorbed, then it will follow the possibility of quantum efficiency to be randomly transfered into a signal or not.

The probability of the PMTs to produce the one photoelectron when the generated photon reaches its surface is defined as:

$$Prob(\lambda, i) = QE(\lambda) \times \frac{A(\lambda, \theta_i)}{A(\lambda, 0)} \times COREPMT \times qetable(i) \tag{45}$$

The parameters in this equation mean:

1. $QE(\lambda)$: the quantum efficiency of 20-inch PMT depending on wavelength of incident photon.

2. $A(\lambda, \theta_i)$: the acceptance of photon on PMT surface, which depends on the wavelength and incident angle. In other words, it represent the possibility for a photon to be absorbed by PMT cathode and no to be reflected or transmitted.

3. COREPMT: a global parameter used for all PMT to correct the average collection efficiency. This is a tunnable parameter and adjusted with LINAC calibration data.

4. $qetable(i)$: the relative quantum efficiency for i-th PMT. This is measured by Ni calibration.

After a photon is successfully transfered into a photoelectron, the output charge follows 1p.e. charge distribution which is made from Ni calibration data. If the output charge exceeds the electronic threshold($\sim 0.2p.e.$), it will be recorded into the data. Finally the time and charge information of all the hit PMTs will be applied with software trigger, which is the same one used for real data.

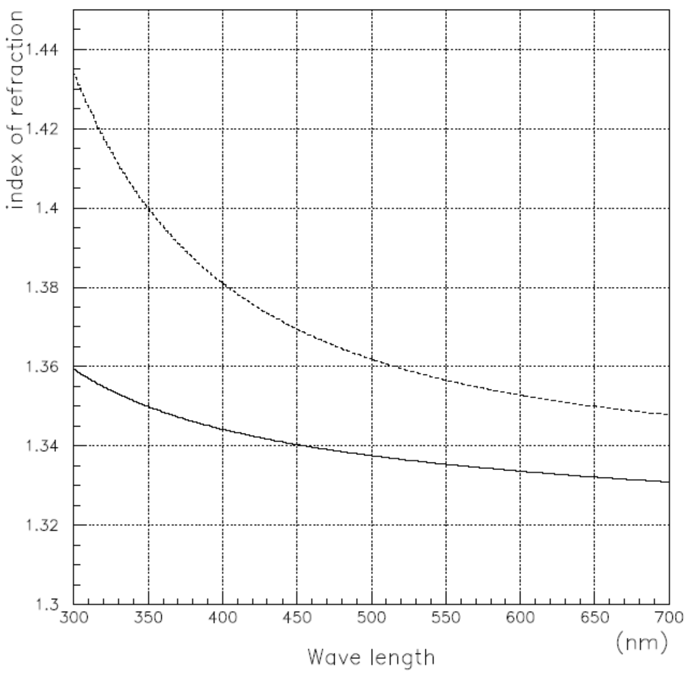

Figure 20: The solid line is refractive index depends on wavelength. The dashed line is the "effective index".

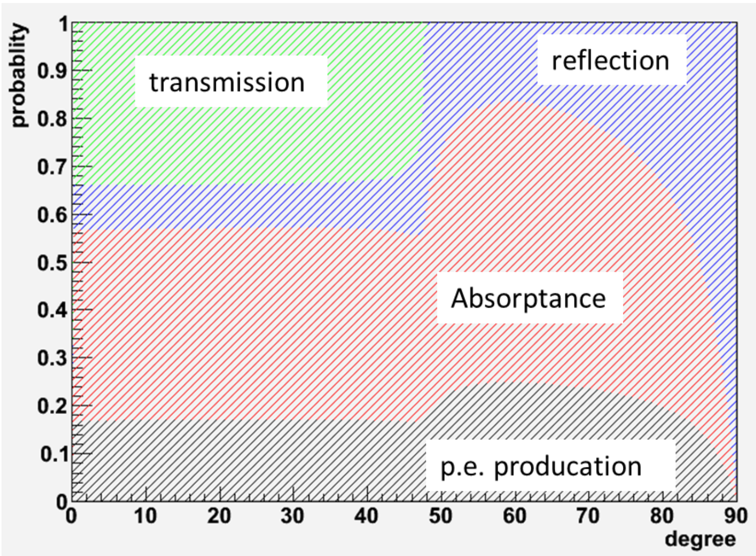

Figure 21: The possibility of absorption, reflection and transmission depending on the incident angle by the case of Unpolarized wave of 345nm.

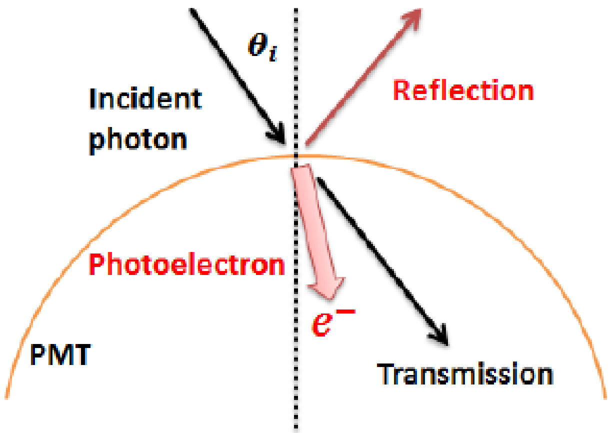

Figure 22: An incident photon hit on PMT surface, it can be reflected or transmitted, or absorbed to be changed into a photonelectron.

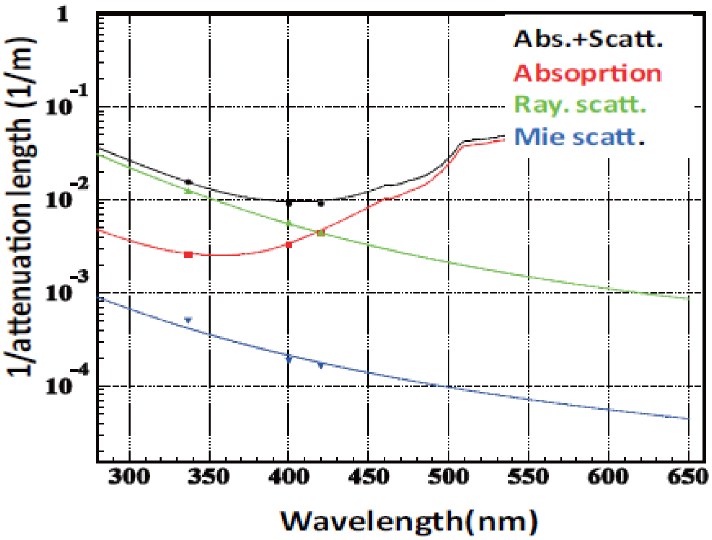

Figure 23: The component of Mie scattering, Rayleigh scattering and absorption in attenuation length in SKdetsim.

4.6 Summary of SKdetsim

4.6.1 Tunable Parameters

Overall, the tunnable parameter in SKdetsim can be summarized below:

Water parameters
The parameters explained in previous section are measured by laser calibration which inject the laser light from tank top, barrel and bottom. There is usually no need to modify these parameters unless the measurement has been updated.

Top-Bottom asymmery
This is not mentioned in previous section. From Ni calibration data it can be found that the hit rate for PMTs in top and bottom has small difference. To reproduce this effect in simulation, SKdetsim has a parameter to correct the top-bottom asymmetric(TBA table). The TBA table is calculated from Ni data, and double-checked by auto-laser calibration measurement.

PMT time resolution and after pulse
Both of the two are tuned in SKdetsim by LINAC calibration data to make PMT time response to be consistent with data. After pulse is the later peak which appear after the main peak in PMT timing distribution. The reason for after pulse is considered as a photoelectron which is back scattered at the first dynode, loses its velocity against the electric field and then comes back to the first dynode to produce a decay hit. The timing distribution tuned by LINAC can be double-checked by Ni calibration data.

COREPMT(global parameter of collection efficiency)
As explained in previous section, COREPMT is a global parameter represent for quantum efficiency of all PMTs. The small difference between PMTs is corrected by the parameter of relative quantum effciency. COREPMT is tuned by LINAC, and relative QE table is made by counting PMT hit rate with Ni calibration data

4.6.2 Some other explanation

For the reader who is interested to make further modification in SKdetsim, some special treatment in SKdetsim program is explained here:

1. SKdetsim is based on Fortran Language, and zebra stream(an old data format with ".zbs" as the suffix of output data file) is used as buffer memory. When a new particle is generated, the information including the particle ID, position, direction, momentum, will be stored in zbs buffer. In tracking step, SKdetsim will read the particle information from zbs buffer and make the tracking one by one. If any secondary particle is produced in tracking, the information will also be stored into zbs buffer, and the tracking of secondary particle will start after the tracking of parrent particle is finished. The only exception is Cherenkov photon. When a Cherenkov photon is made, the tracking of parrent particle will be suspended and the new Cherenkov photon will be tracked immediately. This is because Cherenkov photon can be largely produced and if they are tracked later, the memory is not enough.

2. To save running time, the number of Cherenkov photon is half reduced, and as compensation, the absolute QE, which affected by COREPMT, is doubled from the real number. Attention should be paid to this if someone try to define a High QE PMT in SKdetsim, because the absolute QE is doubled and can exceed 100% to cause bug.

3. When the photon is reflected on PMT surface or black sheet, the photon is actually killed and a new photon with the reflected direction is store into the zbs buffer. Differs from GEANT3, GEANT4 does not kill the photon when reflected.

5 Calibration

5.1 Xe and Ni calibration

Xe and Ni calibration are used to calibrate PMT parameters [30]. In PMT calibration, Quantum Efficiency(QE) and gain are two important factors. Xe calibration is to determine the High Voltage(HV), and Ni caliration is to obtain the absolute gain of each PMT.

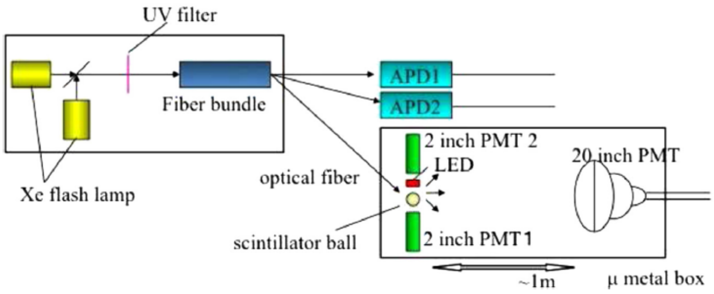

Figure 24: Setup of Xe scintillation light. The optical fibers are connectted to APD and a 20-inch PMT, both for monitoring the light indensity [30].

QE also includes the collection efficiency of photoelectrons onto the first dynode of the PMT. Gain is the conversion factor from the number of collected photoelectrons to output charge (in units of pC). Low energy events like relic neutrino or solar neutrino usually consist of single photoelectron (pe) hits so their analysis heavily depends on QE calibration, while high energy events depend more on gain calibration. The output of the PMT depends on the voltage applied on it. For further explaination, the charge response of one PMT can be defined as:

$$Q_{obs}(i) \propto N_{photon}(i) \times QE(i) \times A(i) \tag{46}$$

Q_{obs} is the charge response finally observed in i-th PMT. $N_{photon}(i)$ is the number of photons hit on the photocathode of i-th PMT. $QE(i)$ and $A(i)$ are the QE and gain of i-th PMT respectively.

So first of all, it is necessary adjust the HV of the PMTs to make sure the PMTs with same geometry will give the same Q_{obs}. For this calibration, Xe flash lamp is used as a light source. Light from the lamp passes through a UV filter and then be injected into the tank through optical fiber, finally arrive at a scintillator ball placed near the center of the tank($(x, y, z) = (353.5, 70.7, 0.0)cm$). The other two fibers go to an avalanche photodiode(APD) module and a dark box installed with a 2 inch PMT, which are both used to monitor the light intensity of Xe lamp. The scintillator ball is an acrylic ball containing 15ppm POPOP as a wavelength shifter and 2000ppm MgO as a diffuser to make the light emission from the ball as uniform as possible. The light emitted from the scintillator ball has the wavelength near to Cherenkov light(peak at 440nm).

The PMTs with the same geometry are divided into one group. In each group, there are standard PMTs which have been pre-calibrated to be used as

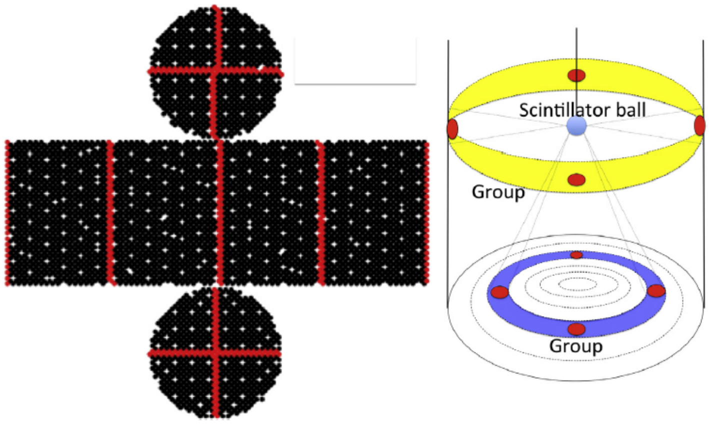

Figure 25: left shows the locations of "standard" PMTs which are indicated by the red points. Right shows the PMT grouping. PMTs with the same geometry are divided into the same group [30].

references for the other ones. After HV calibration, finally the relative difference for the PMT charge response is $\sim 2\%$.

After HV calibration, Ni-Cf source is used to measure the absolute gain. This source is made by ^{58}Ni ball and a ^{252}Cf stick inserted inside the ball. Neutrons are provided by ^{252}Cf, and 9MeV γ rays are emitted isotropically by neutron capture on ^{58}Ni. The source is made like a ball as shown in the Figure 26.

Since more than 99% of observed signals are due to single photoelectron, the result of Ni calibration can be used to determine the factor to convert the charge(pC) to the number of photonelectron. At the begining of SKIV, the factor is determined as $2.645pC/p.e.$.

5.2 LINAC Calibration

The full name of LINAC device is Mitsubishi ML15MIII electron linear accelerator (LINAC) [37], which is used for calibration of the absolute energy. It was originally used to be for medical purpose and was acquired from a hospital then converted into a calibration tool for SK in 1996. It is permanently housed in the dome area above the tank, consisting of a special electron gun, steering magnets and collimators.

LINAC is purposed to produce single electron event, so the steering magnets and collimators are used to control the mono-energetic electron beam. Beam intensity is tunable, and the beam can be collimated such that electrons are injected into the tank at a low enough rate($\sim$0.1 per bunch). Before injecting the beam into the tank, a germanium detector with an hight energy resolution((1.92 keV at 1.33 MeV electron)) is set to measure the beam energy. The Ge detector itself was calibrated by 0.662 MeV monochromatic gamma rays from ^{137}Cs and 9.0MeV gamma from $Ni(n, \gamma)N^*$. Multiple calibration port holes exist on the top of the detector, and the beampipe can be lowered to a variable depth in the detector. In this fashion, many different areas in the detector are accessible and can be calibrated.

Figure 26: The Ni ball for absolute gain measurement. The ^{252}Cf source is inserted as a stick inside the ball [30].

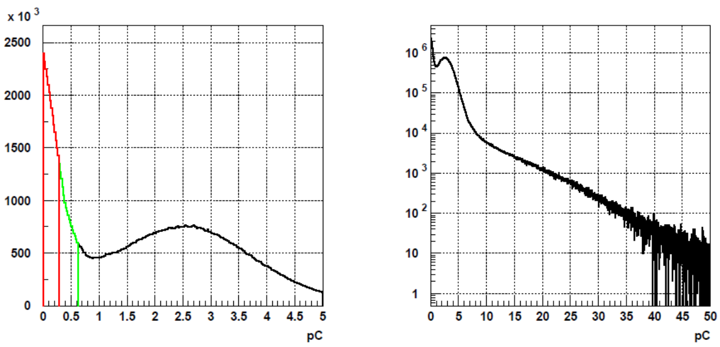

Figure 27: Distribution of 1p.e. charge response in SKIII. The right one is in log scale and left one is in linear scale. Due to the hardware threshold, it is impossible to make measurement to 0pC, so the red line in left figure is a linear fitting.

LINAC calibrations were performed in 2009, 2010, 2012, 2017 and 2018 during SK-IV period. Since the calibration hole positions are fixed and the length of the beam pipe is also fixed, the calibration data were taken at the fixed 6 points as shown in Fig 28.

After the LINAC calibration data is taken, the SK simulation is tuned to match the detector response. Comparing the peak positions in the Neff distributions, COREPMT is determined. After this value is fixed, the difference of Neff between the calibration data and the MC simulation was evaluated and treated as systematic uncertainty.

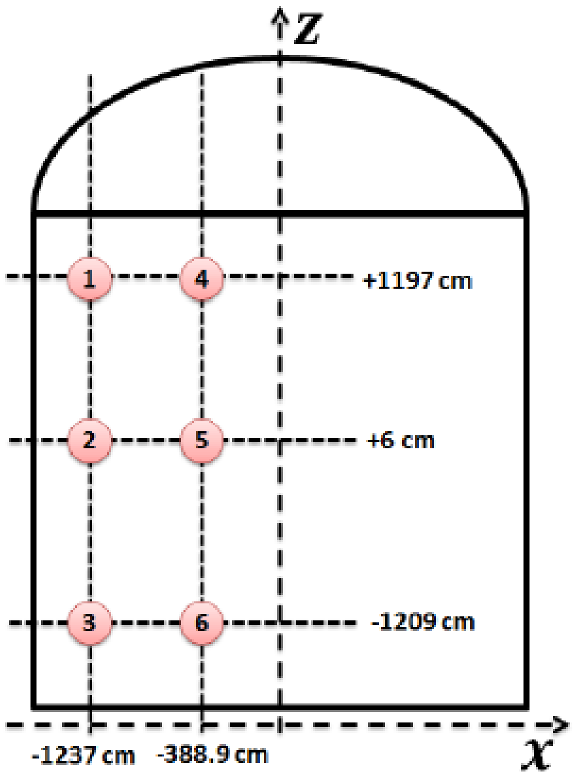

Figure 28: The fixed positions for LINAC data taking.

5.3 DT Calibration

A deuterium-tritium (DT) generator is used to check the absolute energy scale for low energy events [36]. It operates in conjunction with the LINAC, providing a cross check on the energy calibration. It is less time consuming to use then the LINAC and better for monitoring long term stability with frequent checks. Furthermore, the device output is isotropic, and isn't limited to only downward going events like the LINAC, thus allowing study of direction dependent effects.

The generator emits neutrons with the following reaction:

$$^3He +^2 H \rightarrow^4 He + n \tag{47}$$

The energy of the generated neutron is 14.2 MeV and this energy is large enough to create ^{16}N in water as

$$^{16}O + n \rightarrow^{16} H + p \tag{48}$$

The ^{16}N decays via several channels with its half-life of 7.13 seconds. The main decay channels produce a 6.1 MeV γ ray and a 4.3MeV β(66%) and a 10.41MeV β
(28%).

$$^{16}N \rightarrow^{16} O + e^- + \nu_e \tag{49}$$

Although the beta spectrum is spread and it is not good for absolute energy calibration, there are several advantages of the DT calibration over the LINAC calibration. This provides the directional and the positional dependence of energy scale. The directional and positional dependences are important for the solar neutrino analysis, and this is also treated as the systematic uncertainty in solar analysis.

DT data is taken every few months, and the energy scale as determined by the DT agrees with the results of the LINAC calibration to better than 1%. Various positions in the tank are monitored to assure the energy scale at all regions are consistent.

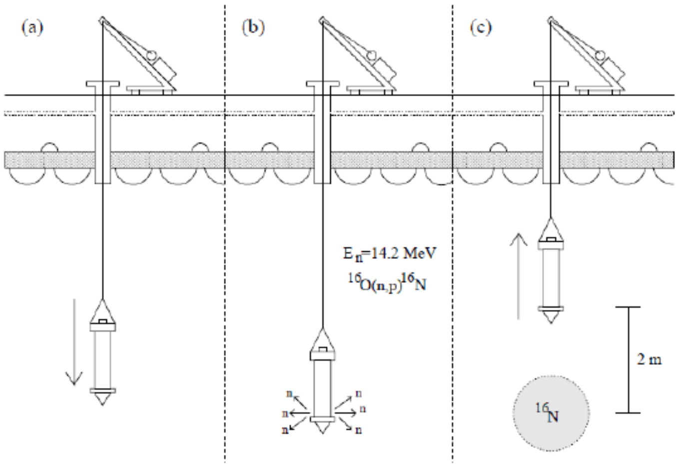

Figure 29: The DT source is like a rocket, and it is put into the tank by a lifter [36].

5.4 Water Transperency

5.4.1 By Laser

Lasers are used to directly measure light scattering and absorption parameters in a wavelengths of 337nm,375nm, 405nm, 445nm and 473nm. The three parameters α_{abs}, α_{sym}, α_{asym} in SK simulation are determined by this measurement. The light is injected every one minute and the hit rate in the different region of the SK ID are monitored. The measurement methods are as following:

1. The detector is divided into 6 regions, top and barrel (B1 to B5 as shown in Fig 30).
2. The scattered hit rate Fig 31 and the observed total charge Q_{total} are measured, then the ratio of hits and Q_{total} $(hits/Q_{total})$ distributions are obtained for each divided region. The observed charges in the bottom PMT are used for the reference to monitor the intensity of the laser light.
3. Several sets of MC simulations are generated with varying the coefficients and the same $(hits/Q_{total})$ distributions are prepared.
4. The distributions of the calibration data and the MC simulation are compared using the χ^2 defined as

$$\chi^2 = \sum_{region} \frac{(Data - MC)^2}{\delta_{data}^2 + \delta_{mc}^2} \tag{50}$$

   Data (MC) is the peak position of $(hits/Q_{total})$ distribution, and δ_{data} (δ_{mc}) is the standard variation of that.
5. Scanning the water transparency coefficients to minimize the value of χ^2.

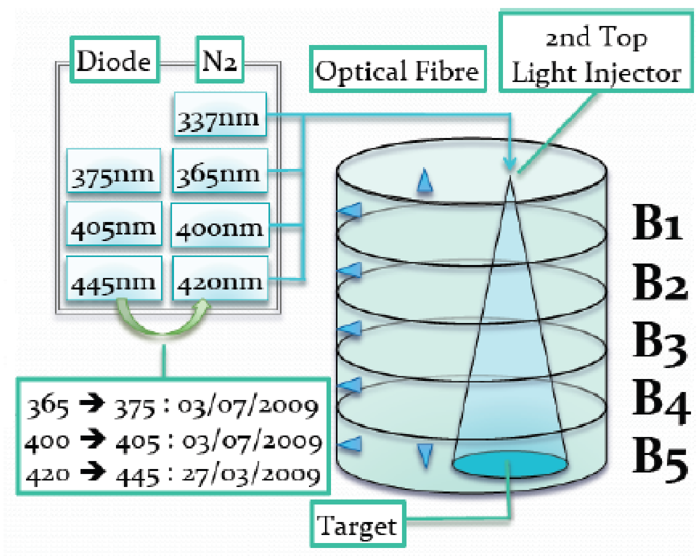

Figure 30: The schematic view of the laser injection system for water parameter measurement [30].

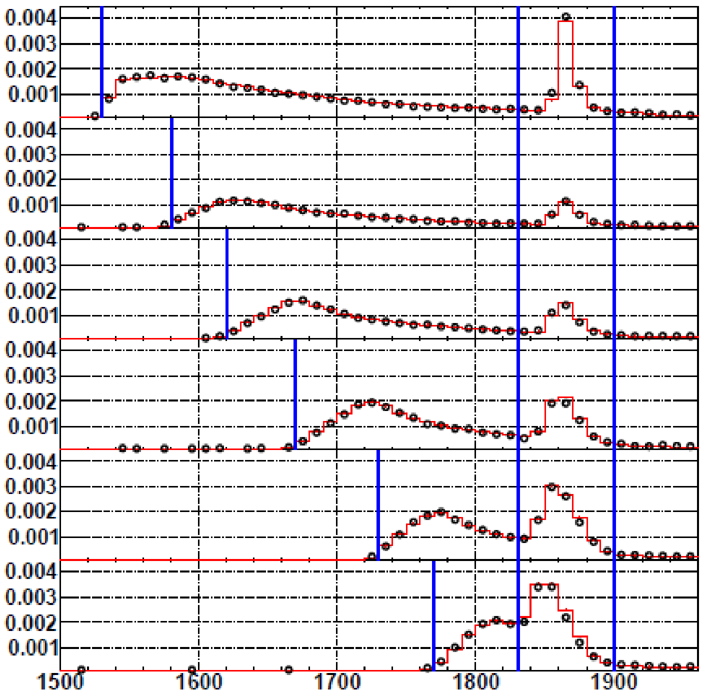

Figure 31: The typical hit rate distribution for each layer. The horizontal axis is the timing after subtracting TOF. The vertical axis is the hit rate. Red line is simulation with best tune, black dot is the real measurement [31].

5.4.2 By decay electron

Cosmic ray muons enter the detector at a rate of about 2 Hz, and about one in 20 will stop in the detector. These stopping muons decay into electrons with the well known Michel spectrum. These decay electrons can be identified by associating the event with a muon that closely near it in time, and whose reconstructed muon stopping point is near to the location of the decay electron vertex. With 10 years of data in SK-IV, a very large sample of the events has been accumulated, which can be used as an independent means of monitoring detector stability, as well as the water transarency change. The selection criteria of decay electron events are following:

1. The time difference between the parent muon event and the decay electron candidate event ΔT, selected as $3.0\mu sec < \Delta T < 8.0\mu sec$.
2. The reconstructed vertex of the decay electron candidate event is within the 22.5kton fiducial volume.
3. The distance between the stopping point of cosmic ray muon and decay electron candidate event is within 250cm.

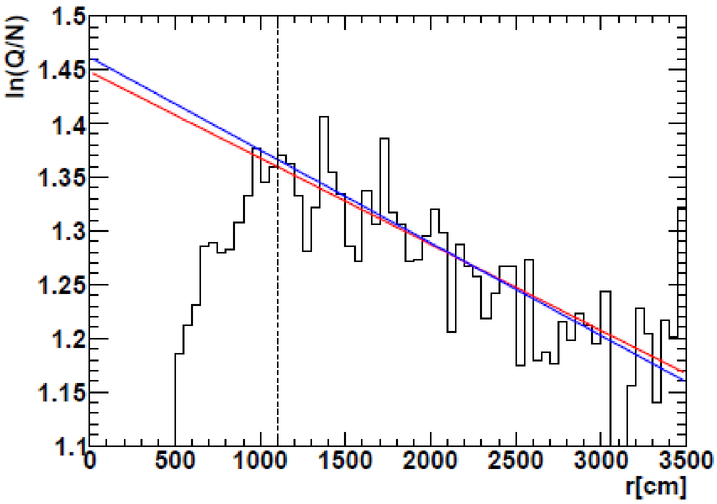

Figure 32: A typical histgram of $ln(Q_{obs})$ vs distance r. The dashed vertical black line corresponds to 1200 cm and a linear fitting can be made above that. The blue line is fitted with a fixed intercept of 1.486 in y axis, red line is fitted with intercept [32].

After selecting the decay electron events, the observed charge $Q_{obs}(i)$ of the i-th PMT and the distance(r) between the i-th PMT and the decay electron candidate are calculated. Then, mean of the observed charge is evaluated as

$$\overline{Q_{obs}} = \frac{\sum Q_{obs}(i)}{N_{total}} \tag{51}$$

The typical histograms of $ln(\overline{Q_{obs}})$ and the mean distance r are shown in Fig 32. To obtain the water transparency, the histograms are fitted by a linear fitting function from 1200cm to 3500cm. The inverse of the slope of the linear fitting function is used as water transparency. Though the result is affected by PMT gain, because if the PMT gain increases, $Q_{obs}(i)$ will also increase, but the PMT gain can be measured by other calibration so this is still a useful method to double-check the water transparency change.

6 Data Set

6.1 Solar neutrino sample and reduction

6.1.1 Bad run selection and bad channel cut

In SK system, it is required to change the run by every 24 hours. And a typical run, which is 24 hours, is usually divided into ∼1100 subruns, whose time length are ∼70 seconds (depending on the trigger rate). Before the reduction process for solar neutrino data sample, the data runs are selected by removing the bad runs to guarantee the data quality. The defination of a bad run is:

1. The run less than 5 minutes will be discarded because the pedestal data is not enough.
2. Sometimes hardware or software problems occured and the DAQ system was stopped. Then the corresponding subrun will be discarded.
3. When the calibration or maintenance is carried out, the DAQ system will be changed to calibration run or test run, these runs will be removed from the solar data sample. Also in normal run, sometimes fake Supernova burst generated by LED is used for training, the correponding subruns are also removed.
4. Sometimes it is necessary to open the tank (for example, LINAC or Ni calibration), thus the high voltage of the electronics will be turned off. When the high voltage is turned on, the dark noise will be higher than usual. Those subruns will be discarded until the dark rate become stable.

Additionally, SK-IV has been running for 10 years, some of the PMTs have bad performance. Currently there are 140(160) bad PMTs in ID(OD) detector. For every month, an average number of bad PMT channels $\overline{N_{bad}}$ will be calculated, the subruns with bad channel $N_{bad} < 10$ or $N_{bad} > \overline{N_{bad}} + 1.5 \times 24$ are removed. This is because most of the short runs do not have enough data to estimate bad channels so the calculated N_{bad} is small, and for some case, the QBEE board get out of order and the 24 PMTs connected to the QBEE board are treated as bad channels.

6.1.2 Pre reduction

The events observed in SK is $\sim 2 \times 10^5$ per day. Most of them are backgrounds, with 295 elastic scattering events from solar neutrinos are expected in one day. The size of raw data is $\sim 100GB$ per day, so it is necessary to remove most of the obvious background events in the first reduction step before go into the final sample. Though the cut criteria applied in this step is very loose, data size and event number are largely reduced. The details of the cut criteria is:

fiducial volume cut The fidualcial volume cut refers to the 2m distance cut from ID wall. This is intended to remove the events whose reconstructed vertex position is close to the wall, because a good reconstruction quality can not be expected near the wall, as the photon reflection on the PMT and black sheet surface can cause the problem. The inner tank has a radius of 16.9m and a height of 18.1m, which means this cut removes the events with $R > 14.9m$ or $|z| > 16.1m$, and keep the fiducial volume as 22.5kton, equal to 70% of the inner volume.

energy cut and OD cut
To keep the low energy range($4 \sim 20MeV$) for solar neutrino, events with more than 2000 hit PMTs will be removed, as those events are too energitic and they are usually cosmic muons. For the same purpose, events with OD trigger flag are also removed, because an expected elastic scattering event of solar neutrino is impossible to make an OD trigger. The events with reconstructed energy lower than 4MeV are also removed, since low energy background is dominate below that.

loose external gamma cut
The major background in low energy range is the gamma ray from the rock around SK detector, or the radioactivity from the detector structure itself. These background events have two features: The vertex are close to the wall; The direction goes inward. To use these two features, firstly the vertex and direction are reconstructed. Then the position P_{wall} is calculated by going from the vertex to the wall through the opposite reconstructed direction. The distance d_{eff}, which is the distance from the vertex to P_{wall}, is used for loose external gamma cut as the events with $d_{eff} < 400cm$ are removed. Here we use the word "loose" because more tighter and optimaized cut will be applied in later process.

loose reconstruction quality cut
As mentioned before, the parameter g_V is used to estimate the quality of vertex reconstruction and the possibility of misfit. g_d is for that of direction reconstruction. In first reduction, events with $g_v^2 - g_d^2 > 0.1$ is removed.

Time difference cut
This cut removes the event which is too close to the previous LE trigger by $\Delta T < 50\mu s$. Those events can be considered as three kinds of background:

1. The ringing effect from very high energy muon. This usually happens in $1\mu s$ after the muon event.
2. Decay electron from cosmic muon. The half-life of muon is $2.2\mu s$.
3. After pulse caused by PMT electronics. In time distribution, after pulse usually makes a peak right after the real event, but it can also make the peak as late as $15\mu s$.

6.1.3 Spallation cut

The cosmic muons are energitic enough to break the oxygen nucleus and leave radioactive elements in tank water. Such radioactive impurity decays in the water, and they refer to spallation backgrounds. The reactions occur between cosmic muon and oxygen nucleus are complicated and can be written as:

$$\mu +^{16} O \rightarrow \mu + X + \cdots \quad (52)$$

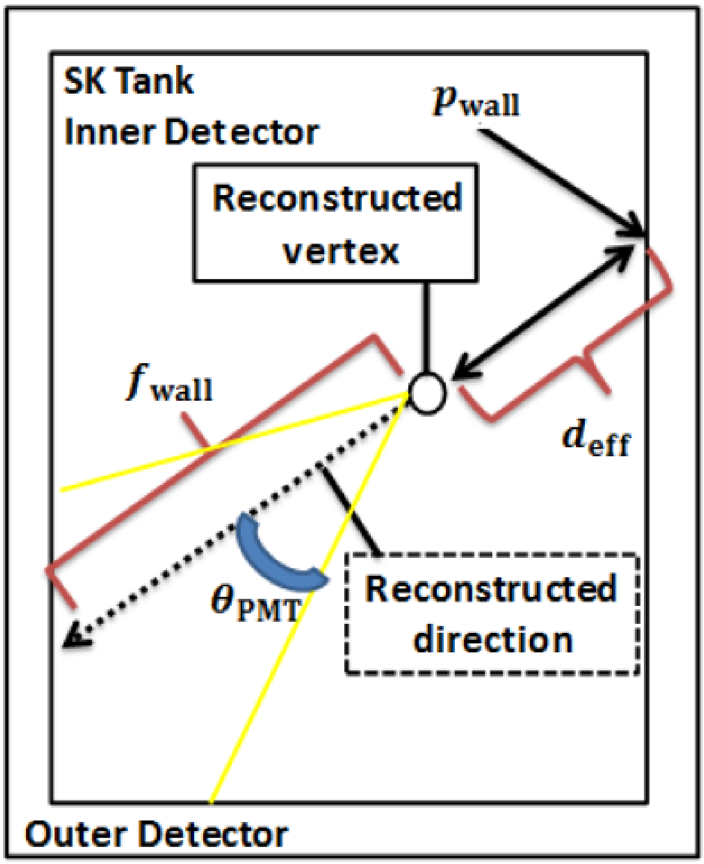

Figure 33: Explanation of the defination of d_{eff}, p_{wall}, f_{wall} and θ_{PMT}.

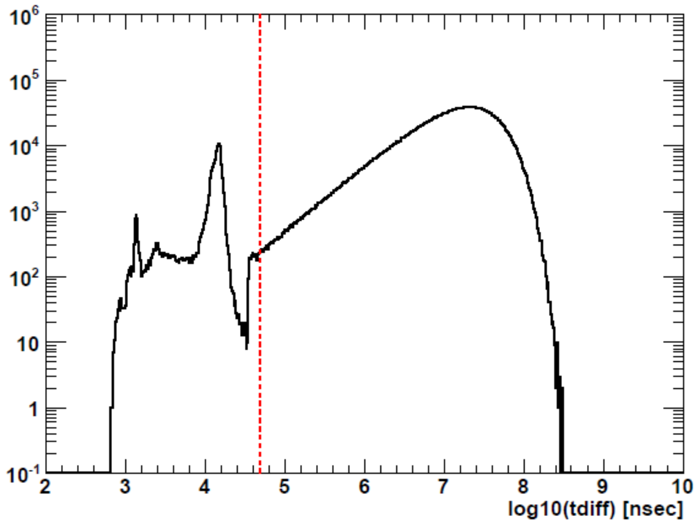

Figure 34: The distribution of time difference to previous LE triggered event. The red dashed line represents for the cut point of $50\mu sec$ cut. The peak around $1\mu sec$ is caused by ringing effect after high energy cosmic muons, the peak around $15\mu sec$ is considered to be caused by after pulse [32].

Here X is the radioactive necleus produced by breaked oxygen. In the case that hadrons($\pi^{\pm}$,n,p,etc) are knocked out, they can hit on other oxygen nucleus and cause secondary or thirdary interactions. The radioactive products decay to release β or γ rays, and especially some of the decay products are neary to the solar neutrino energy range, which cause the difficulty to remove the spallation background. The products already known are summarized in the table below. The most long-life one can be up to 13.9sec.

The basic method for spallation cut is:

For each low energy event, find all the muons in previous $50\mu s$ window.

For each pair of muon and spallation candidate, calculate the time difference ΔT and the distance ΔL from the vertex of spallation candidate to the reconstructed track of the corresponding muon.

For the corresponding muon, calculate the residual charge Q_{ref} by substracting the expected charge along the reconstructed muon track. In Equation 53, L is the length of reconstructed muon track, while in most cases the muon pass through the tank and then L is equal to the distance of enter point and exit point. Q_{unit} is the expected charge in unit length of muon track. Q_{unit} is from the average of muon sample, by projecting all the hit PMTs to the track. As the PMT gain increases by time, the parameter Q_{unit} also need to be updated to the lastest one.

$$Q_{res} = Q_{total} - Q_{unit} \times L \tag{53}$$

When spallation or oxygen nucleus breaking occurs, usually some additional photons can be expected, and thus the residual charge Q_{res} will be larger than a clean muon.

Make the likelihood from ΔT, ΔL and Q_{res} with Equation 54.

$$\mathcal{L}_{spa} = P(\Delta t) \times P(\Delta L) \times P(Q_{res}) \tag{54}$$

The PDF for ΔL and Q_{res} are made from a spallation sample whick is selected by $\Delta L < 0.1$ and $E > 8MeV$. The PDF for ΔT is generated by considering all the known radioactive products. To set the cut point of likelihood, the spallation sample is compared with a random sample in Figure 37. The random sample consist of the pairs of a low energy event with $E < 5MeV$ and a random muon. The reason for selecting random sample by $E < 5MeV$ is that below 5MeV the events are mostly caused by radioactive sources from the wall or the detector structure itself, but not by spallation. As shown in Figure 37, in the lastest solar sample, the cut point for spallation likelihood is set at $\mathcal{L}_{spa} = 4.52$ and 88.8%(20.0%) of the spallation-like(non-spallation) events are removed by this cut.

Isotope	$\tau_{1/2}$ [sec]	decay mode	Kinetic Energy [MeV]
$^{8}_{2}$He	0.119	β^- β^-n	$9.67 + 0.98(\gamma)$ 16%
$^{8}_{3}$Li	0.838	β^-	~ 13
$^{8}_{3}$B	0.77	β^+	13.9
$^{9}_{3}$Li	0.178	β^- β^-n	13.6(50.5%) ($\sim$ 50%)
$^{9}_{6}$C	0.127	β^+n	$3 \sim 15$
$^{11}_{3}$Li	0.0085	β^- β^-n	$16 \sim 20(\sim 50\%)$ $\sim 16(\sim 50\%)$
$^{11}_{4}$Be	13.8	β^-	11.51(54.7%) $9.41 + 2.1(\gamma)(31.4\%)$
$^{11}_{4}$Be	13.8	β^-	11.71
$^{12}_{5}$B	0.0236	β^-	13.37
$^{12}_{7}$N	0.0110	β^+	16.32
$^{13}_{5}$B	0.0174	β^-	13.44
$^{13}_{8}$O	0.086	β^+	13.2 or 16.7
$^{14}_{5}$B	0.0138	β^-	$14.55 + 6.09(\gamma)$
$^{15}_{6}$C	2.449	β^-	9.77(36.8%) $4.47 + 5.30(\gamma)$
$^{16}_{6}$C	0.747	β^-n	~ 4
$^{16}_{7}$N	7.13	β^-	10.42(28.0%) $4.29 + 6.13(\gamma)(66.2\%)$

Figure 35: The list of Spallation production [38].

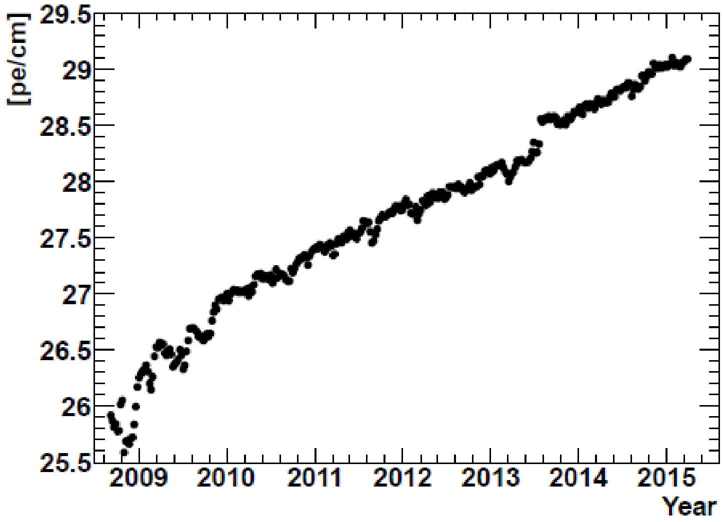

Figure 36: The increasing of Q_{unit} by year.

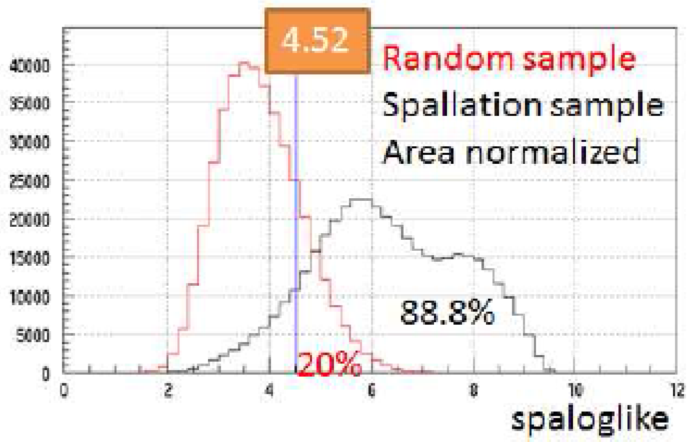

Figure 37: The distriution of final likelihood result for random sample and spallation sample. The horizontal axis is the log of likelihood. By setting the cut point at *spaloglike* > 4.52, 88.8% of spallation sample are removed [34].

6.1.4 ^{16}N cut and other cut

When a low energy μ^- enter the tank, it can be captured by oxygen nucleus and produce ^{16}N. ^{16}N has a half-life of 7.13s and goes beta decay in water, the main decay channel gives a 6.1MeV γ and a 4.3MeV β(66%) and a 10.41MeV β(28%). Both of them are made from muon, but different from spallation, ^{16}N backgrounds have the following features: the muon should be a stoppping one in the tank, which means it has an enter point but no exit point; the vertex and timing of the following low energy event should be close to the stopping muon.

$$^{16}N \rightarrow^{16} O + e^- + \nu_e \tag{55}$$

Since a stopping muon is much more rare than a passing-througn one, a simple cut is more efficient than building a likelihood. So the cut criteria is set as follows:

1. For each low energy event, pick up the previous muon by $Q_{total} > 1000p.e.$, as long as the constrain that the muon has no exit point.
2. Calculate the muon stopping position by the enter point and reconstructed direction/momentum. Cut the low energy event if the vertex is in 250cm range from muon stoppint position when their time difference is also less than 30sec.

Since this is the last step before the solar final samle, some other tight cuts are also applied in this step, which includes:

1. PMT hit number cut
   This cut removes the events whose total number of hit PMTs(N_{total}) is larger than 400. This is because N_{total}=400 corresponds to ~60MeV in case of a recoil electron, when N_{total} exceeds 400, it becomes too energitic for solar neutrino.
2. Tight fiducial volume cut
   Though the 2m distance cut from the ID wall has already been applied in first reduction step, in 3.5-5.0MeV energy range, there still remains background near the bottom and the barrel. As an non-uniform distributed background will cause a large uncertainty in solar analysis, additional vertex cut is applied in 3.5-5.0MeV range:

   $$z > -7.5m \ \ (4.5 - 5.0MeV) \tag{56}$$

   $$(x^2 + y^2) + (\frac{150.0}{11.75^4} \times |z - 4.25|^4) < 150.0 \ \ (3.5 - 4.5MeV) \tag{57}$$

   After the tight cut, fiducial volume is 8.85kton and 16.45kton for 3.5-4.5MeV and 4.5-5.0Mev respectively. There is no additional cut needed above 5MeV.
3. Tight external cut
   As discussed in the part of tight fiducial volume cut, the radioactive background is non-uniformly distributed and most of them are near the wall.

Those low energy background can be considered from the decay of Rn daughters.

To reduce the external signals, the same parameter d_{eff} is used for cut above 5MeV:

$$\begin{cases} d_{eff} > 650cm \ \ (5MeV < E < 7.5MeV) \\ d_{eff} > 400cm \ \ (E > 7.5MeV) \end{cases} \tag{58}$$

Which can be known from Figure 38, the radioactive backgrounds in 3.5-5.0MeV concentrate near the bottom and barrel. Thus the additional cut in this range is defined by p_{wall}. p_{wall} means the position on the wall when tracking from the reconstructed vertex along the opposite direction. p_{wall} is categorized into top, bottom or barrel, and the cut is applied as:

$$\begin{cases} d_{eff} > 1000cm \ \ (p_{wall} = top) \\ d_{eff} > 1200cm \ \ (p_{wall} = barrel) \\ d_{eff} > 1300cm \ \ (p_{wall} = bottom) \end{cases} \tag{59}$$

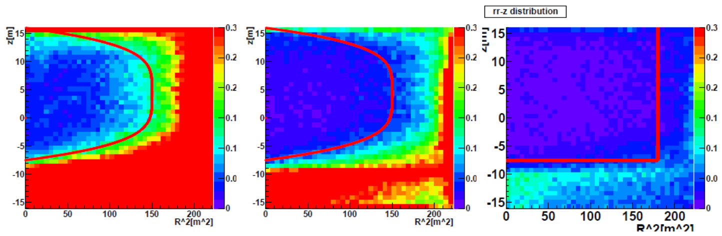

Figure 38: The vertex distribution for 3.5 $\sim$ 4.0 MeV(left), 4.0 $\sim$ 4.5 MeV(middle) and 4.5 $\sim$ 5.0MeV (right) in kinetic energy [32].

4. Cluster hit cut

   When a radioactive event occurs on the PMT surface or FRP cover, it can cause hits on neighbour PMTs. Usually the number of hit PMTs is small but sometimes the event accidentally coincides with dark noise hits and it can be recorded in data. Such event has the features of: Some of the hits clusters near one PMT; About half of the hits are from dark noise, so the sharpness of timing distribution is worse than a real neutrino signal event.

   To cut these events, two parameter are defined:

   (a) R_{02}: The minimum radius containing more than 20% of hit PMTs within 20 nsec time window.

   (b) N_{20rawT}: The maximum number of hits in a 20ns timing window(without subtracting T_{tof}).

   For convienence, another parameter C_{lik} is defined as:

$$C_{lik} = R_{20} \times N_{20rawT}/N_{eff} \tag{60}$$

By comparing the background with solar neutrino MC simulation, the cut criteria is set as:

$$\begin{cases} C_{lik} < 75.0,\ r^2 > 155m^2,\ z < -7.5m\ \ (4.5MeV < E < 5.0MeV) \\ C_{lik} < 75.0,\ r^2 > 120m^2,\ z < -3.0m\ or\ z > 13.0m\ \ (3.5MeV < E < 4.5MeV) \end{cases} \tag{61}$$

5. Tight event quality cut
   Tight event quality cut uses the same parameter(g_v and g_d) with first reduction step, and the cut criteria is optimized with MC simulation as a signal to ensure the maximum significance $Significance = \frac{Signal}{\sqrt{Background}}$.

$$\begin{cases} g_v^2 - g_d^2 > 0.29\ \ (3.5MeV < E < 5.0MeV) \\ g_v^2 - g_d^2 > 0.25\ \ (5.0MeV < E < 7.0MeV) \\ g_v^2 - g_d^2 > 0.20\ \ (E > 7.0MeV) \end{cases} \tag{62}$$

6. Hit pattern cut
   Solar analysis is searching for the recoil electron from the neutrino, so it is necessary to find a way to distingush γ ray or signals with multiple rings. The γ ray can induce Compton scattering by many times and it will final give a very dirty ring, which actually consist of many rings from the scattered electron. While for a recoil electron event, it usually has a clean ring and the vector from vertex to hit PMT has $\sim 42°$ angle to the track. To use this feature, likelihood for hit patter is defined as:

$$\mathcal{L}_{pattern}(E, \vec{v}) = \frac{1}{N_{50}} \sum_{i}^{N_{50}} log(P_i(E, cos\theta_{pmt}, f_{wall})) \tag{63}$$

   Here N_{50} is the maximum number of hit PMTs in 50ns time window, E is reconstructed energy, θ_{pmt} is the angle between the track and the vector from vertex to hit PMT. f_{wall} is the distance from vertex to nearest wall. P_i is the PDF made from MC simulation of single electron events. By maximum the significance, the cut point is set as:

$$\begin{cases} \mathcal{L}_{pattern} > -1.88\ \ (6.0MeV < E < 7.5MeV) \\ \mathcal{L}_{pattern} > -1.86\ \ (7.5MeV < E < 11.5MeV) \\ \mathcal{L}_{pattern} > -1.95\ \ (E > 11.5MeV) \end{cases} \tag{64}$$

6.2 Relic neutrino sample and reduction

6.2.1 Spallation cut

The spallation background has already been introduced in solar section, but the spallation cut method in relic analysis is different from that in solar analysis. The reason is solar analysis concentrate on the energy range of 4∼20MeV, while relic analysis is looking for neutrino between 16∼30MeV. Since the energy range is different, so the expected radioactive isotopes are also differenet. This means the likelihood built for solar analysis can not been used for relic sample directly. Thus, spallation cut method for relic is developped independently. The basic

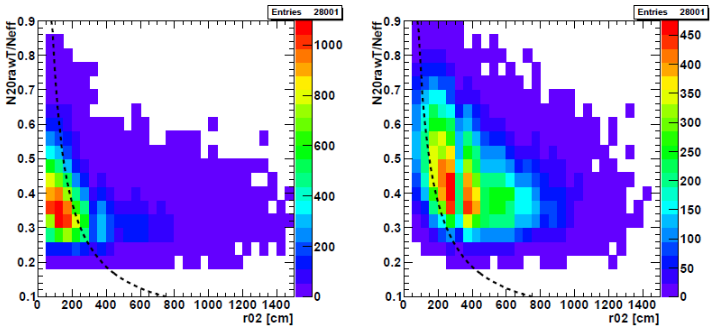

Figure 39: Histogram of r_{02} vs N_{20rawT}. The left is the background sample and the right is the solar simulation result [32].

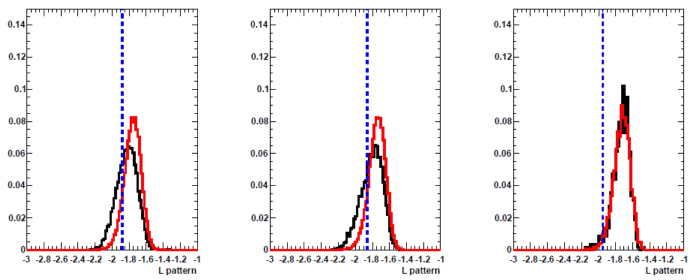

Figure 40: Distribution of hit pattern likelihood. Black is for real data, and red is the simulation of solar neutrino, for 5.5 $\sim$ 7.5MeV in left, 7.5 $\sim$ 11.5MeV in middle, and 11.5 $\sim$ 19.5MeV in right.

thinking is similar, but the likelihood and the variables used for likelihood are defined in another way.

The highest energy spallation product believed to be produced in the detector is ^{11}Li and ^{14}B, each with beta decay end point energies of up to 20.6 MeV. Because of energy resolution effects, events with reconstructed energy up to 24 MeV are reasonable to be suspect to be spallation background.

Luckily, ^{11}Li and ^{14}B have short half-life of around 0.01 seconds, so they are rather easy to associate with the muon which created them. But when we go lower in energy, the number of possible isotopes increases rapidly, as do their half-lives. The basic idea to remove the spallation events is similar to solar analysis, to check the correlations between the electron candidate and the proceeding muon tracks. There are four variables used in searching for the spallation activity:

1. ΔT. The time difference between the electron candidate and the proceeding muon. This is very powerful in identifying short-lived spallation products. The smaller the ΔT, the greater the likelihood that an event being spallation.

2. L_{tran}. The transverse distance from the electron candidate to the muon track. The spallation products are created along the muon track and in general they can not travel far before decaying. A short L_{tran} indicates more possibility of spallation.

3. L_{long}. Firstly, the point where the electron candidate lies on the muon track will be found. Then the peak position of dE/dx plot on muon track will be found. L_{long} is the distance between the two. This is because the spallation occurs on muon track intends to make a peak on dE/dx plot. L_{long} is not as powerful as L_{tran}, but still useful. Since the physics behind spallation has not been fully understood, especially that the hardron physics occur in spallation process can be complicated. So the spallation longitudinally may deserve further investigation.

4. Q_{peak}. The amount of light seen in the peak of dE/dx plot in a bin of 4.5m width. The strong peak Very strong peaks, which show that lots of light was deposited in the detector originating from that region of the muon track, usually indicate spallation.

Since the relic candidates is not as much as solar candidates, Brute Force Fitter(BFF) is also used for muon reconstruction. BFF is also a muon fitter but the reconstructed vertex will be tried in all of the tank by steps which is small enough. BFF cost much more time than Muboy, so it is not unrealistic to be applied to the large number of solar candidates, but can be tried on the limited number of relic candidates.

The result of Muboy will be first tried, when the recontruction precision of Muboy is poor($Goodness$ < 0.4), the result of BFF will be used instead. If both of Muboy and BFF($Goodness$ < 0.3) are not trustable, all the events in 2s window behind the muon will be banned as dead time. Additionally, when the muon is too energitic($totallight > 400,000 p.e.$), all data after the muon will also be rejected for a few seconds. If both of Muboy and BFF are good, then both of their result will be input to calculate the likehood and either of the two looks like spallation, the event will be rejected.

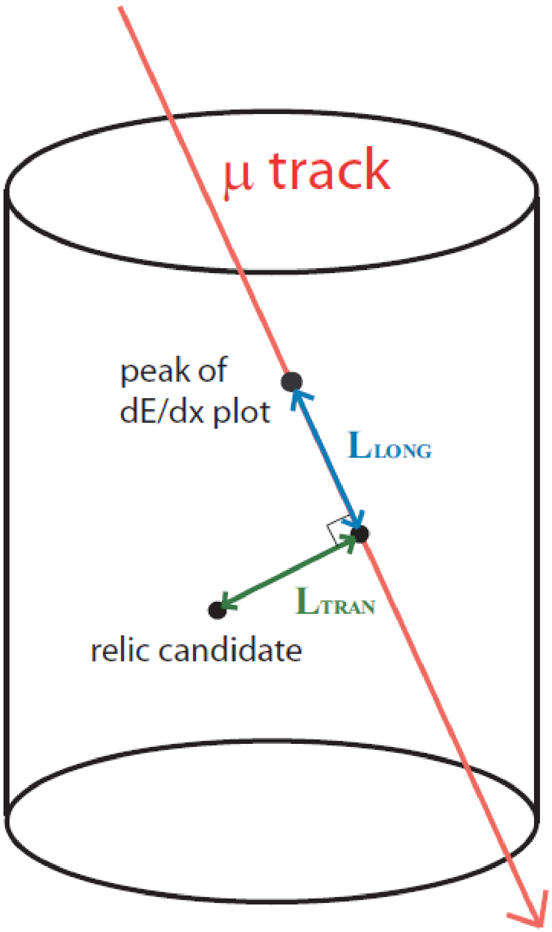

Figure 41: Explanation of the defination of L_{TRAN} and L_{LONG} .

In order to build the likehood, a spallation sample and a non-spallation sample are needed. Since the amount of spallation events are much more larger than the real relic events we can expect, all the proceeding muons occuring with 30 seconds before the candidate events are used as the spallation sample. And the muons occuring within 30 seconds after the candidate events are used as the random sample as they are impossible to have spallation correlations with the candidate events. Distributions of ΔT, L_{tran}, L_{long}, Q_{peak} are made independently and be normalized to make PDFs for the four variables.

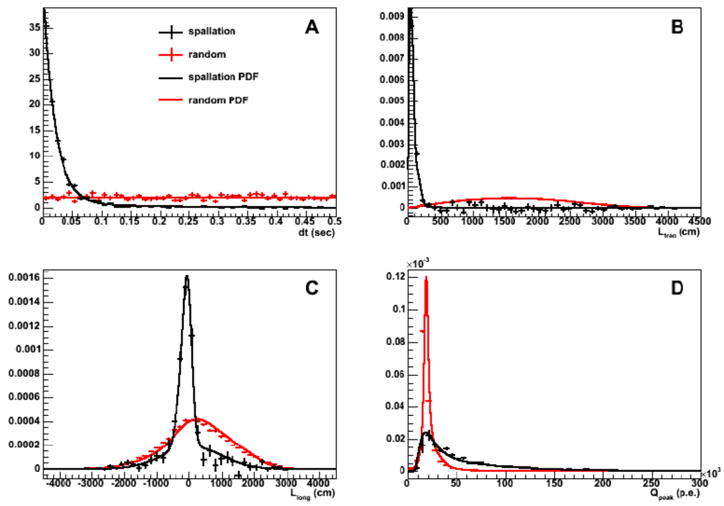

Figure 42: PDF of the four varibles. Red is random sample, and black is spallation sample [63].

Muboy categorize the muon as four kinds: single through-going, stopping, multiple, and corner clipper. The likelihood is built seperately in different energy range, as well as for the four categories as:

$$L_{spal} = log[\frac{P^{spal}_{\Delta T}}{P^{rand}_{\Delta T}} \times \frac{P^{spal}_{L_{TRAN}}}{P^{rand}_{L_{TRAN}}} \times \frac{P^{spal}_{L_{LONG}}}{P^{rand}_{L_{LONG}}} \times \frac{P^{spal}_{Q_{PEAK}}}{P^{rand}_{Q_{PEAK}}}] \tag{65}$$

For muon with multiple track, the likelihood is also seperated for each track and the one with largest L_{spal} will be used for cut. The likelihood is the primary way that spallation events are eliminated, and some cuts on specific quantities also exist.

6.2.2 2peak cut

Although most decay electrons are eliminated by the $50\mu sec$ pre cut, occasionally it occurs that the muon decays quickly enough that both the muon and the decay electron information are captured in the same $1.3\mu sec$ timing window that comprises a single event. In these cases, the timing information for that event will have a double peak structure. Other, even rarer events can cause multiple peaks as well. The cut purposed to remove such kind of events is the so-called 2peak cut or pre/post activity cut.

In order to find and reject such events, the timing information of the event was searched for any indication of a peak outside the main timing peak. The algorithm uses the BONSAI fit time to define the main peak. Any hits with time of flight subtracted times earlier than 12ns before main peak is considered as possible pre-activity; any time after 20ns after the BONSAI event time is considered post activity.

For each of the 3 regions (pre-activity, main, and post-activity), the peak is searched by scanning the maximum hit inside a 15ns time window. The maximum hit number in each region is recorded as N_{15}. In the final stafe, if N_{15} in pre-activity region is more than 12, or N_{15} in post-activity region is more than 15, then the event is rejected.

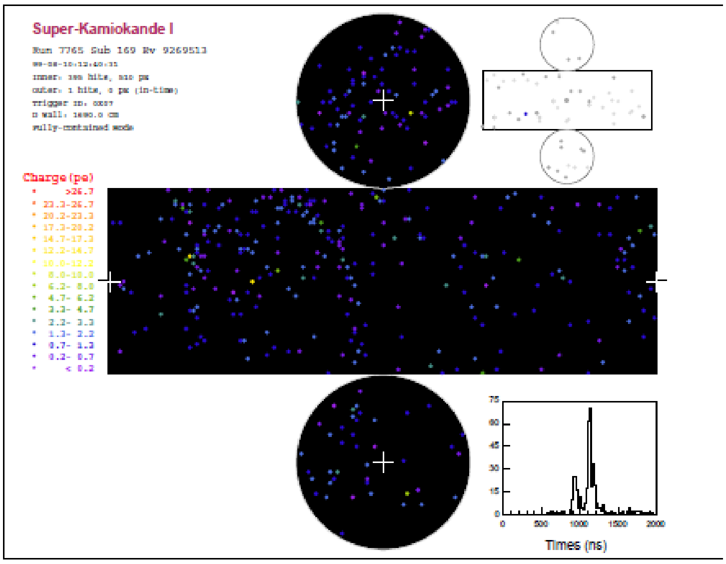

Figure 43: An example event withe 2 peaks.

6.2.3 Multiple ring cut

Atmospheric neutrino events can produce multiple charged particles by the interaction with water. As the multiple charged particles may share the same timing peak, such events can not be removed by the pre/post activity cut. These multiple charged events can have multiple Cherenkov rings.

To remove these specifically, we use the fact that these multi-particle events have multiple Cherenkov rings, A ring counting method has already been developed for SK atmospheric neutrino analyses utilizing Hough transforms, We used the same method to look for multi-ring events. The software determines an angle between the rings we can use. In rare cases overly fuzzy electron rings can be mistaken for two different rings by the software; for this reason events determined to be multi-particle, but separated by less then 60 degrees, were kept, while events with multiple rings separated by more then 60 degrees were rejected.

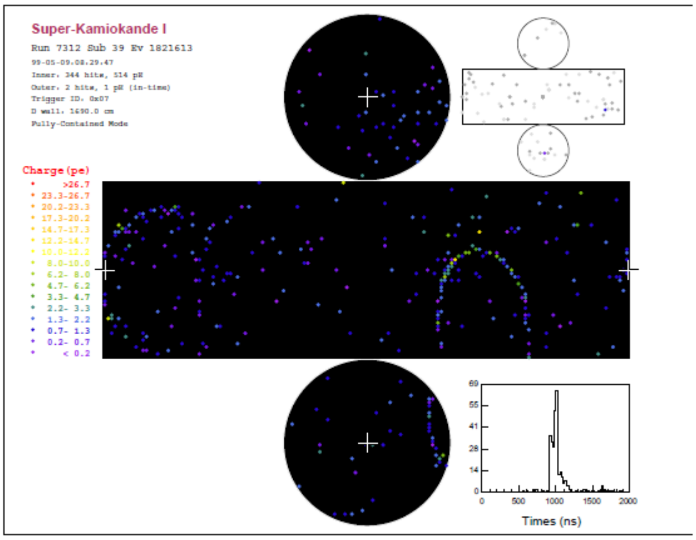

Figure 44: An example event with multiple rings.

6.2.4 Cherenkov angle cut

For a typical single electron event, or other Charged particles traveling close to the speed of light in pure water emit Cherenkov light in a cone shape with an opening angle of about 42 degrees. While for low momentum heavier particles, such as muons, pions, and nucleons created by atmospheric neutrinos, they can also be reconstructed in the relevant energy region by tagged as an electron. However, in that case those particles produce Cherenkov light with an opening angle that is smaller then 42 degrees. For γ ray, since multiple scattering can confuse the ring, so the Cherenkov angle distribution is not as sharp as we could hope. As a result, the reconstructed Cherenkov angle for γ event is usually much larger than 42 degrees.

Fig 45 shows the Cherenkov angle distribution of SN relic MC (LMA model). The main peak is determined to be between 38 and 50 degrees, and this is the cut applied to the data to eliminate remaining heavy particles at lower angles, and more isotropic events at higher angles. As the signal region is defined between 38 and 50 degrees, the Cherenkov angle cut is also useful in further removing spallation events that are due to a β decay plus a γ emission.

6.2.5 Pion cut

When it goes to relatively high energy range($E > 30MeV$), most of the events are actually pions created by atmospheric neutrino interactions. Since the pions are much heavier and they are usually quickly captured by Oxygen and disappear, pions intend to give the Cherenkov ring to be cleaner and sharper

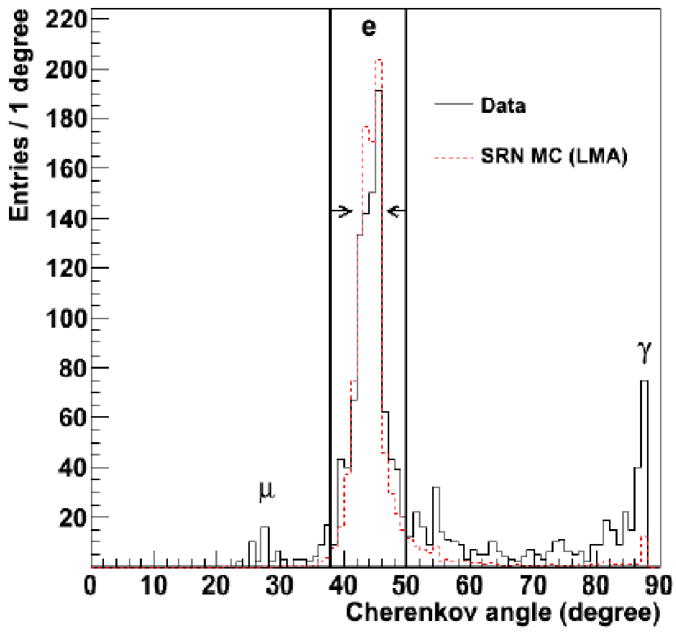

Figure 45: Distributions of the Cherenkov angles for the data(black) and SRN simulation(red).

than electron, because when an electron is travelling in water it will suffer from multiple scattering and the direction will be slightly changed, which results in a relatively poor and dirty ring, but much better than a γ signal.

The 'fuzziness' or 'sharpness' of the Cherenkov ring can be considered for discriminating pions and electrons. To quantitatively estimate that, the distribution of the cone angles from three-hit combinations which is made in Cherenkov angle fitting can be used. This distribution will be narrower for pions then for electrons, though the two peak at the same angle. Using this logic, a pion likelihood variable was constructed, where pion likelihood is defined as follows:

$$L_{PION} = N_{entries}^{\pm 3^\circ} / N_{entries}^{\pm 10^\circ} \tag{66}$$

$N_{entries}^{\pm 3^\circ}$ is the number of entries in $\pm 3^\circ$ range from the peak. $N_{entries}^{\pm 10^\circ}$ is the same meaning for $\pm 10^\circ$. By looking at SN relic MC compared to pion MC, the cut criterion was determined to be 0.58, which makes the cut approximately 1% inefficient.

6.3 Atmopheric neutrino sample

The high-energy data sample has three different categories: fully-contained (FC), partially-contained (PC), and upward-going muon (UPMU) [66]. FC neutrinos have reconstructed interaction vertices inside the fiducial volume of the inner detector, combined with low light levels in the outer detector. PC neutrinos also have interaction vertices inside the fiducial volume, but have significant light in the outer detector volume indicating exiting particles. UPMU neutrinos are the highest-energy SK sample; they result from muon-neutrino interactions in the rock surrounding the detector, which produce penetrating muons. These muons either stop in the inner-detector volume as stopping events, or go through the inner detector as through-going events. The energy range for neutrino parents in FC and PC sample is 100 MeV–10 GeV, and for UPMU it is 1.6 GeV–100 PeV.

7 Neutrino search for GW170817

7.1 GW170817 overview

On August 17th 2017 at 12:41:04 UTC, the Advanced LIGO and Advanced Virgo experiment identified the first evident signal of a gravitational wave from the binary neutron star merger, named GW170817 [2]. The interpretation is a merger of two compact objects consistent with neutron stars having total system mass of 2.74 solar masses and a luminosity distance of 40 Mpc. Associated with this gravitational wave signal, the Fermi Gamma-ray Burst Monitor and International the Gamma-Ray Astrophysics Laboratory also detected a short gamma-ray burst, GRB170817A, which has a consistent location with the merger and a 1.7-s delay to the merger time [1]. Subsequent extensive electromagnetic follow-up observations in ultra-violet, optical and infrared wavelengths were performed. These observations led to the conclusion that the merger happened in galaxy NGC4993 and was followed by a short gamma-ray burst and a kilonova/macronova [3, 4]. High-energy neutrino signals associated with the merger were also searched for by the ANTARES, IceCube, and Pierre Auger Observatories. It was concluded that no significant neutrino signal was observed [5].

A search for neutrinos in Super-Kamiokande (SK) associated with this gravitational wave signal produced by the binary neutron star merger in NGC4993 will be reported in this section. The analysis method is similar to that for the previous neutrino search in SK for GW150914 and GW151226 [6].

As mentioned in previous sections, in SK analysis neutrino events with reconstructed energies above 100 MeV are categorized as the 'high-energy data sample', which are typically used to study atmospheric neutrinos and to search for proton decay. Neutrino events with reconstructed energies below 100 MeV and down to 3.5 MeV are categorized as the 'low-energy data sample'. They are typically used to study solar neutrinos and to search for core-collapse supernova neutrinos. The directional determination accuracy varies according to sample and direction, but can be as accurate as $\sim$1 degree for upward-going muons. Some theoretical predictions of neutrino emission mechanism via binary neutron star mergers have been proposed; for example, some fraction of the kinetic energy in relativistic ejecta from gamma-ray bursts could convert to high-energy ($\sim 10^{14}$ eV) neutrinos, or a similar mechanism as for core-collapse supernovae could produce few-tens-of-MeV neutrinos [7, 8], the expected fluence is roughly estimated to be 10^4 cm^{-2} for 10 MeV neutrinos within 1 second after merger. Neutrino observations associated with a binary neutron star merger using the unique characteristics in SK would validate such proposed mechanisms. Coincident search was made in the full data sample using the same time window as ANTARES-IceCube-Pierre Auger, i.e., $\pm$500 s around the merger time and in a 14-day time window relevant for longer-lived emission processes [5]. The primary background events for this search in the high-energy data sample are almost entirely atmospheric neutrinos, while radioactive impurities, spallation products from cosmic ray muons, atmospheric and solar neutrinos are the main backgrounds in the low-energy data sample. We note that SK carried out a LINAC calibration from August 3-22, 2017. Fortunately, physics data-taking operated at the time when the neutron star merger occurred; however, there were unavoidable radioactive impurities adhered on the surface of the LINAC beam pipe present in the low-energy data sample.

7.2 Search method and result

As mentioned before, the energy range for neutrino parents in FC and PC sample is 100 MeV–10 GeV, and for UPMU it is 1.6 GeV–100 PeV. All the three event topologies are considered for this search. Further information about the selection and reconstruction methods for the three categories can be found in reference.

	observed num. of event	expected num. of event
	in ± 500 s	
FC	0	$(9.36 \pm 0.06) \times 10^{-2}$
PC	0	$(7.52 \pm 0.23) \times 10^{-3}$
UPMU	0	$(1.64 \pm 0.02) \times 10^{-2}$
	following 14 days for all sky	
FC	76 ± 8.72	91.44 ± 0.57
PC	8 ± 2.83	7.35 ± 0.23
	following 14 days for 5° solid angle	
UPMU	0	$(6.11 \pm 0.04) \times 10^{-2}$

Table 7: The numbers of expected and observed events in FC, PC and UPMU data sets, respectively, for a $\pm$500-s time window around GW170817 and for 14 days after GW170817. The errors on the observed number of events in the following 14 days for the entire sky are $\sqrt{N}$. For UPMU event search in following 14 days, the event number in a solid angle of $\pm 5^\circ$ around NGC4993 was shown instead. The energy range for FC and PC is 100 MeV–10 GeV, and the energy range for UPMU is 1.6 GeV–100 PeV. The total livetime for the following 14 days is 11.30 days.

A $\pm$500-s window search around the LIGO detection time of GW170817 has been conducted. Since the observation of optical light and gamma ray burst lasted for 14 days, a 14-day window search following the GW detection was also carried out. These two kinds of time windows are consistent with those neutrino experiments in reference.

$\pm$500-s window search In the $\pm$500-s window around GW170817, no neutrino event was found in the FC, PC, or UPMU data sets. This null result is used in the calculation of the upper limit on neutrino fluence in the next sections.

For lowe energy signals, there are 7 events found after solar reduction($3.5 \sim 16MeV$) and no event was found after SRN reduction($16 \sim 100MeV$). However, the LINAC calibration was carried out in that period. At the timing of GW170817, beam was not running but the pipe was inside the tank.

In Super-K regular calibration, the events reconstructed inside 2m space from the calibration source are removed for solar or relic neutrino search. After checking the vertex of the 7 events in solar sample Fig 46, all the 7 events found in solar sample are considered to be from the impurities of the pipe surface and thus no signal was for GW170817.

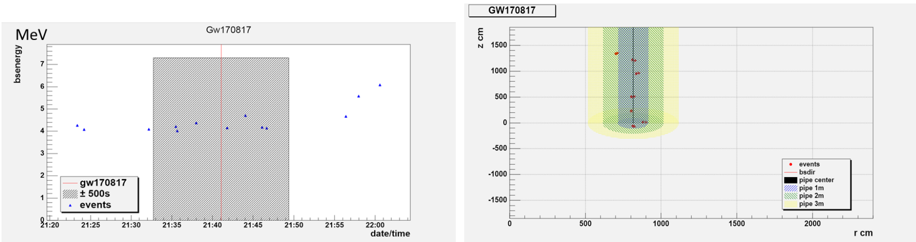

Figure 46: The left shows the timing(horizontal axis) and reconstructed energy(vertical axis) of the 7 events found in ±500-s window(shadow box) of solar sample. The right is the reconstructed vertex of the 7 events, while the horizontal axis is $r = \sqrt{x^2 + y^2}$ and the vertical axis is z. The yellow shows the 2m space from the center of LINAC pipe. All the 7 events found are considered to be from the impurities of the pipe surface.

14 days window search Since the LINAC calibration was carried out in that period, there are too many noise events in low energy range. These noise events are not only from the beam, but also can be from the impurities of the pipe or the electronics noises, because the tank was opened and closed very frequently, as well as the pipe was moved in and out, and the hardware electronics were turned on and off. Thus, it is difficult to make physics study on the low energy sample for the 14 days window and the result will not be used for this search.

For high energy sample, the event numbers found in 14 days window is summarized in Table 7. The expected number of events in Table 7 based on 2976.01 days of SK data. The livetime for the high-energy analysis is 11.30 days, after removing LINAC beam runs in the following 14 days after GW170817.

Unlike the FC and PC samples, the UPMU sample only contains upgoing muons, so it is sensitive to only half of the sky. In 60.4% of the following 14 days, NGC4993 is within the sensitive half. Since the direction of NGC4993 is well known [3,4], for UPMU data, for which the angular resolution is better than for the other two samples, we concentrated on a ±5° cone around NGC4993 for the event search in the following 14 days. This method was previously used in SK to search for neutrino signals associated with astrophysical objects [9]. The 5° constraint was not used for the ±500-s search in Table 7 because no event was observed in all sky during this window, and unlike the 14-day-window case, the zenith angle change of NGC4993 in ±500-s can be ignored. All the results listed in Table 7 are consistent with our expected event rates and no significant signal was found for GW170817.

7.3 Fluence limit

Though there is no event observed within a ±500-s window, either in low-energy data nor in high-energy data, the null number can be converted to an upper limit on neutrino fluence. The calculation for neutrino fluence limit is done separately for the low-energy, FC+PC, and UPMU data sets. The calculation uses the same procedure laid out in [10], which follows from [11].

FC+PC ($100MeV \sim 10GeV$) For the FC and PC data set, the neutrino fluence can be calculated using equation (67),

$$\Phi_{FC,PC} = \frac{N_{90}}{N_T \int dE_\nu \sigma(E_\nu)\epsilon(E_\nu)\lambda(E_\nu^{-2})}, \tag{67}$$

N_{90} is the 90% C.L. limit calculated from a Poisson distribution, for the observed neutrino events in a $\pm$500-s window with the expected background number. Since there is no neutrino event found in a $\pm$500-s window, N_{90} can be fixed as $N_{90} = -\ln(0.1) = 2.3$. N_T is the number of target nuclei relevant to the neutrino interactions, while for Charge Current Quasi-Elastic reaction and Neutral Current Quasi-Elastic reaction, the target is Oxygen. σ is the combined cross section for all interactions as plotted in Fig 47. ϵ is detection efficiency as shown in Fig 48, and λ is the density of E_ν assuming an energy spectrum with index of -2 as shown in Fig 49. This spectral index is commonly assumed for astrophysical neutrinos accelerated by shocks [12].

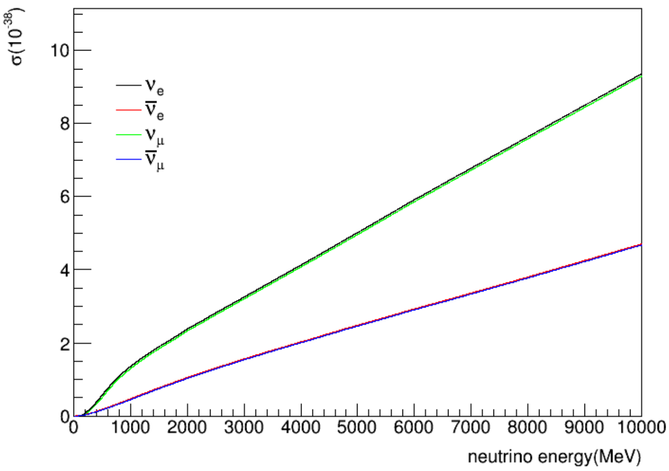

Figure 47: The cross section for all interactions combined in the range of $100MeV \sim 10GeV$. Colors represents the four differenet neutrino types included in FC and PC data.

Fluence limits are calculated separately for each neutrino type because the cross section and detection efficiency depend on neutrino type.

Cross sections in equation (67) are from NEUT 5.3.5 [13]. NEUT 5.3.5 is also used to produce mono-energetic neutrino interactions in the SK Monte Carlo detector simulation in order to determine the detection efficiency.

low energy ($4MeV \sim 100MeV$) The fluence calculation for low-energy neutrinos uses an expression similar to (67) but with different energy spectra. Here we assume two kind of spectra, one with an index of 0, i.e., a flat spectrum, and another being a Fermi-Dirac distribution with average energy of 20 MeV. The two kind of spectrum are plotted in Fig 50.

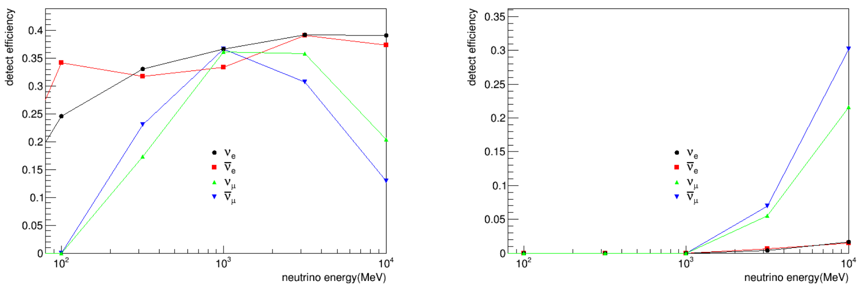

Figure 48: Detection efficiency for the four neutrino types in FC and PC data. Left is for FC, and fight is for PC. It need to be noticed that the Cherenkov threshold for muon is 157.4MeV so there is no sensitivity for ν_μ and $\overline{\nu}_\mu$ near 100MeV in FC. To produce PC events, usually more energetic neutrino is needed so the sensitivity is near 0 below 1GeV.

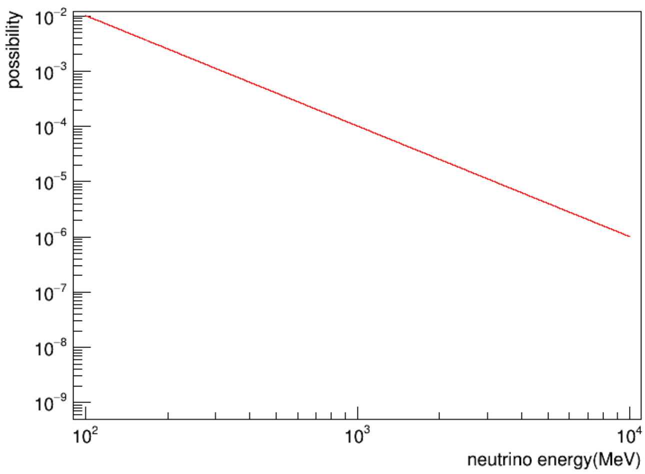

Figure 49: The energy spectrum used in FC+PC fluence limit calculation. It is assumed with a index of -2 and normalized to make total are to be 1.

$$\Phi_{lowe} = \frac{N_{90}}{N_T \int dE_\nu \lambda(E_\nu)\sigma(E_\nu)R(E_e, E_{vis})\epsilon(E_{vis})}, \tag{68}$$

R is the response function to convert electron or positron energy (E_e) to kinetic energy in SK (E_{vis}). R is estimated by SK detector Monte Carlo simulation explained in previous section. $\epsilon(E_{vis})$ is the detection efficiency. $\epsilon(E_{vis})$ depends on the detected energy, and was estimated for $4 \sim 20MeV$ by solar reduction method and $20 \sim 100MeV$ by SRN reduction method, respectively. The combination of $R(E_e, E_{vis})$ and $\epsilon(E_{vis})$ is shown in Fig 51. Again, no event was observed in ± 500 s, so N_{90} is 2.3.

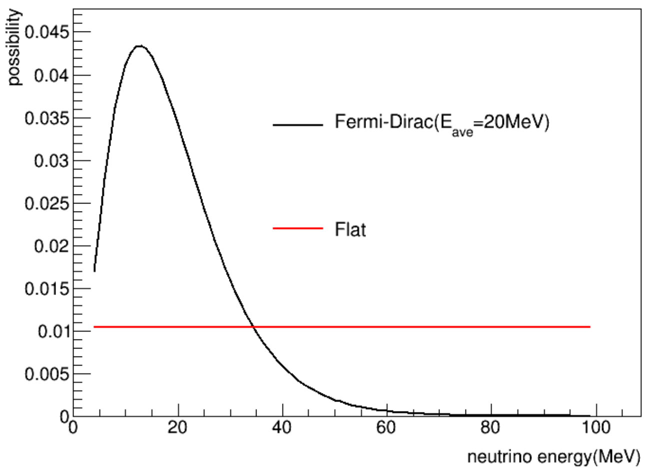

Figure 50: The energy spectrum used in low energy fluence limit calculation. A flat spectrum and a Fermi-Dirac distribution with average energy of 20 MeV are used. Both the two are normalied to make total area to be 1.

We also express the fluence limit which is calculated for monochromatic neutrino energy E_ν. The fluence limits at various energies are shown in Figure 52.

UPMU **(**$1.6GeV \sim 100PeV$**)** For the UPMU data set, the neutrino fluence is calculated using equation (69),

$$\Phi_{UPMU} = \frac{N_{90}}{A_{eff}(z) \int dE_\nu P(E_\nu)S(z, E_\nu)\lambda(E_\nu^{-2})}. \tag{69}$$

The fluence of UPMU events depends on zenith angle. $A_{eff}(z)$ is the zenith-dependent effective area (shown in Fig 54), where z is the the zenith angle of the incoming neutrino. $P(E_\nu)$ is the probability for a neutrino to create a muon which is higher than E_ν^{min} and thus can be detectable in SK. $P(E_\nu)$ for ν_μ and $\overline{\nu}_\mu$ are shown in Fig 55 respectively. $S(z, E_\nu)$ is the shadowing of the neutrinos due to interactions in the Earth (shown

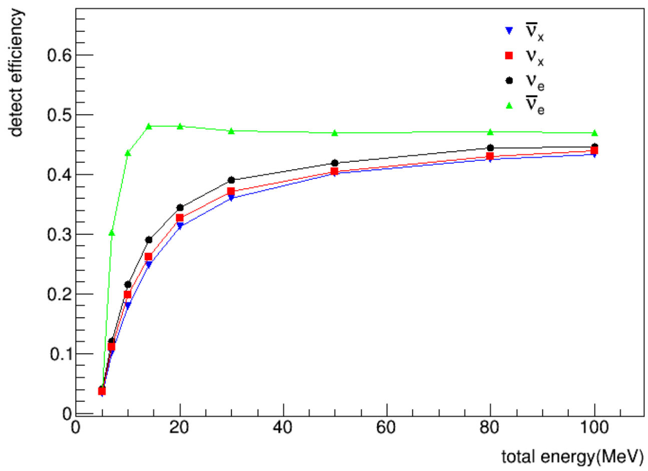

Figure 51: Detection efficiency for lowe energy range. This refers to the combination of $R(E_e, E_{vis})$ and $\epsilon(E_{vis})$ in Equation 68.

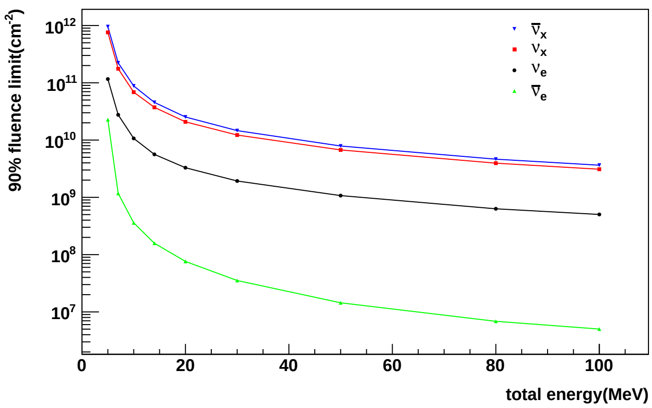

Figure 52: The 90% C.L. limits for GW170817 events on fluence obtained for mono-energetic neutrinos at 4 MeV, 7 MeV, 10 MeV, 14 MeV, 20 MeV, 30 MeV, 50 MeV, 80 MeV and 100 MeV.

in Fig 56). $S(z, E_\nu)$ also depends on zenith angle because when $cos(z)$ is getting close to 1, the travel distance in the earth is getting longer and less neutrino can reaches SK detector. Similar to FC and PC limits, λ here is the number density of E_ν in a spectrum with index of -2.

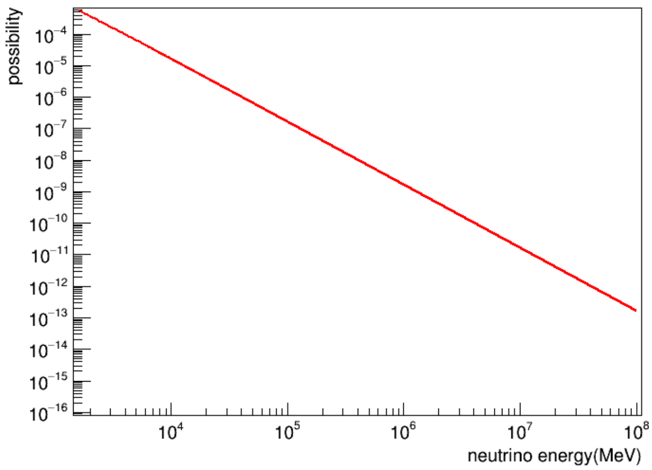

Figure 53: The E^{-2} spectrum used in the calculation for fluence limit of UPMU data.

The results of fluence limits for FC+PC, UPMU, and low-energy data are summarized in Table 8. The UPMU upper limit fluence values range from (14–37) cm^{-2} for neutrinos and from (18–50) cm^{-2} for antineutrinos, depending on zenith angle from 90° to 0°. The zenith-dependent upper limit of neutrino fluence from UPMU events are shown as a sky map in Figure 57. As mentioned before, UPMU data set collect the upgoing muon events and thus it only has sensitivity to half of the sky. Fortunately at the detected timing of GW170817, the source NGC4993 is in the sensitive half.

To focus on the direction of NGC4993, UPMU limit is $16.0^{+0.7}_{-0.6}$ cm^{-2} and $21.3^{+1.1}_{-0.8}$ cm^{-2} for neutrinos and antineutrinos, while the error is calculated by a range of $\pm 5°$ around the zenith angle of NGC4993.

We note that the present study is sensitive to neutrinos between 1.6 GeV and 100 GeV, which is not covered in other searches [5]. Our UPMU data may be compared or combined directly with that of other neutrino telescopes. We provide an UPMU fluency limit in Figure 58. It need to be stressed that SK has the best limit for neutrinos below 100MeV, which is the expected energy range of thermal neutrinos from binary neutron star merger.

Considering d_{GW} as the distance from the detector to NGC4993, our upper limit on fluence of UPMU data can be converted into an upper limit on total radiated energy in neutrinos, by weighting by $4\pi d^2_{GW}$ in equation (69). The resulting upper limit on total energy is $E_\nu^{\rm tot}$ $\sim$(1–6)$\times 10^{53}$ ergs for GW170817 assuming the luminosity distance of 40 Mpc.

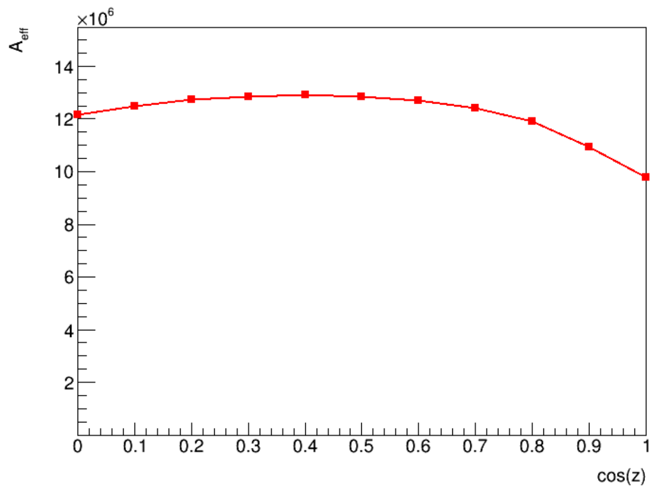

Figure 54: Effect area which depends on zenith angle.

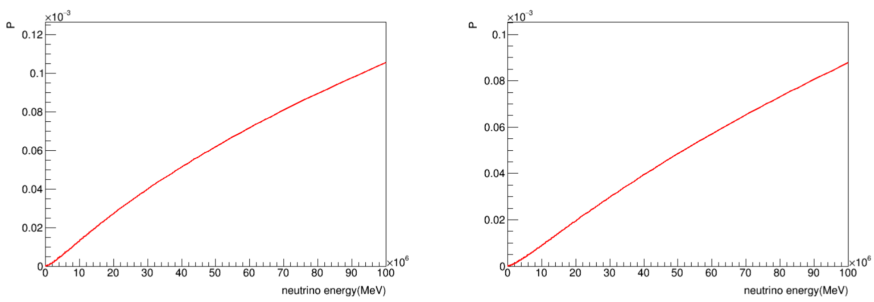

Figure 55: The possibility for a neutrino to produce a detectable muon in SK, which refers to $P(E_\nu)$ in Equation 69. Both the detection efficiency and cross section are included.

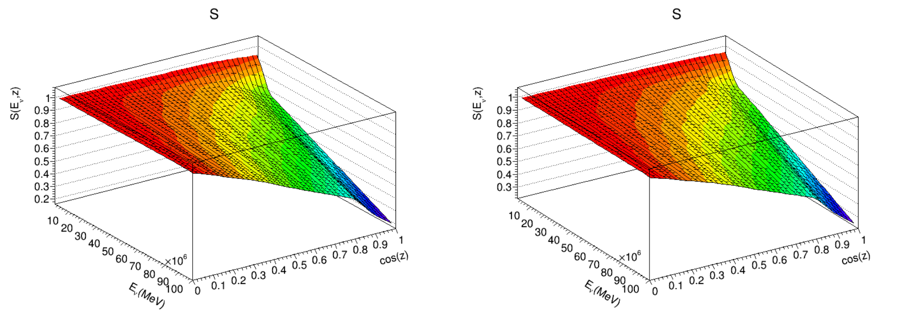

Figure 56: S in Equation 69, which can be considered as the possibility for the neutrino to interact in the earth. The left is for ν_μ and the right is for $\overline{\nu}_\mu$. S depends on neutrino energy and zenith angle, as different zenith angle means different distance for neutrino to travel from the back of the earth.

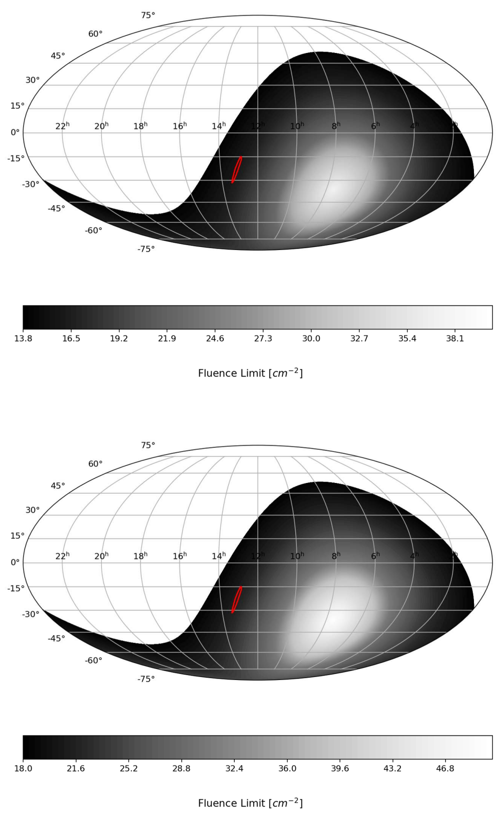

Figure 57: The 90% C.L. limit on fluence for neutrinos(left) and antineutrinos(right) in UPMU data set, overlaid with the 90% C.L. contour for the location of GW170817 according to LIGO and Virgo released data (solid red line).

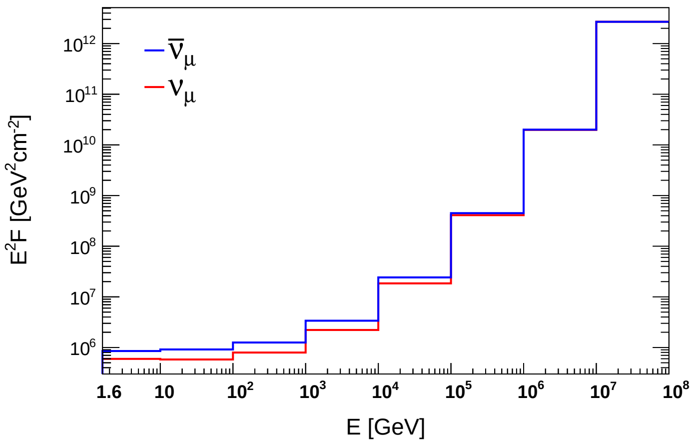

Figure 58: The 90% C.L. limits for the UPMU data set during a ±500-s window, in the direction of NGC4993. Limits are calculated separately for each energy range, by assuming a spectrum with index of −2.

	GW170817 $\Phi_\nu(\text{cm}^{-2})$	
	from FC+PC only	**from UPMU only**
ν_μ	5.6×10^4	$16.0^{+0.7}_{-0.6}$
$\bar{\nu}_\mu$	1.3×10^5	$21.3^{+1.1}_{-0.8}$
ν_e	4.8×10^4	-
$\bar{\nu}_e$	1.2×10^5	-
	from low-energy only	
	flat spectrum	Fermi-Dirac with E_{ave}=20 MeV
$\bar{\nu}_e$	1.2 $\times 10^7$	6.6 $\times 10^7$
ν_e	1.0 $\times 10^9$	3.4 $\times 10^9$
$\bar{\nu}_x$	7.5 $\times 10^9$	2.6 $\times 10^{10}$
ν_x	6.3 $\times 10^9$	2.1 $\times 10^{10}$

Table 8: Limits at 90% C.L. on the fluence of neutrinos from GW170817 given a spectral index of −2 and a range of 100 MeV–10 GeV for FC+PC and 1.6 GeV–100 PeV for UPMU data. The error of UPMU limit is made with ±5° range around zenith angle of NGC4993. Low-energy limits assume a flat spectrum as well as a Fermi-Dirac spectrum with $E_{average}$=20 MeV from 3.5 MeV to 100 MeV. $\nu_x(\bar{\nu}_x)$ represents $\nu_e(\bar{\nu}_e)$ and $\nu_\mu(\bar{\nu}_\mu)$.

8 De-excitation gamma search from Charge Current Quasi-Elastic reaction

8.1 Motivation and Plan

This research focus on the search for de-excitation γ from CCQE interaction of atmospheric neutrino and the direct measurement of the Branching ratio($Br(\gamma)$). De-excitation γ has been briefly introduced in Section 1. To explain the motiavtion more clearly, when an atmospheric neutrino induce CCQE interaction with Oxygen inside SK, a muon and a possible $\sim 6MeV\gamma$ will be produced. As the product muon can be above or below Cherenkov threshold and the de-exicitation γ can be given or not given, the final signal observed in the detector can be considered to have four categories:

1. The muon energy is below the Cherenkov threshold and thus invisible, and no de-excitation γ is emitted. In this case, no prompt signal can be observed, and the only signal is the decay electron from the invisible muon, but since there is no visible signal to tag the electron, it is impossible to know whether it is a decay electron from muon or an electron from neutrino, and thus this will be a unreducable background component for low energy neutrino analysis.

2. The muon is invisible, but de-excitation γ is emitted. In this case, firstly the de-excitation γ is observed, after the invisible muon decays with a half-live of $2.2\mu sec$, there will be a decay electron. By searching for the pair of a prompt γ and a delay electron, a sample of the de-excitation γ can be obtained

3. The muon is energetic enough to give Cherenkov light in SK water, but there is no de-excitation γ emitted. Since the muon is produced inside the tank, such kind of events are saved in FC set of ATMPD data sample, and the decay electron is saved in the $-5 \sim +35\mu sec$ window.

4. The muon is visible, and de-excitation γ is emitted. similar to 3 case, this kind of events is saved in FC data set and the decay electron is saved in the $-5 \sim +35\mu sec$ window.

For case 3 and 4, a coincident search for a delayed electron can ensure that the muon is from CCQE interaction. Additionally, by search the γ signal inside the prompt muon event, case 3 and case 4 could be distingushed and thus the branching ratio of de-excitation γ could be obtained. A possible method which can be used for γ search inside muon will be introduced in following section.

For case 1, only decay electron can be observed, thus it is impossible to distingush it from the expected electron signal from either the IBD interaction or the elastic scattering. The energy of decay electron follows the Michel Spectrum and can be up to $\sim 60MeV$, which overlaps the search window of Supernova Relic Neutrino($16 \sim 30MeV$). As a result, this is an unreducable background component in SRN search. Besides, this component does not affect the solar neutrino analysis, because solar neutrino search focus on $4 \sim 20MeV$ window which is rather little in Michel Spetrum, and further more they could be removed by solar angle cut($cos(\theta_{sun}) > 0.8$).

The background component from case 1 is the motivation of this study. This is one of the two most difficulties in SRN search(another is spallation background), and can also make an uncertainty term in long base long neutrino experiment. Though this kind of background is not countable, if we can directly measure the branching ratio of de-excitation γ, then it will be possible to estimate this background component.

For case 2, a pair of a prompt γ and a delayed electron is expected. By the coincident search of the prompt and delayed signal, this case is countable and a sample of de-excitation γ can be made. Supposing the $Br(\gamma)$ is already known, by counting case 2, case 1 can be esimated.

To specify a detailed plan for this study, the following steps are considered:

1. Use simulation to establish the method of searching for a γ inside a muon event.

2. Search for the coincident signal of a prompt γ and a delayed electron to make a sample of de-excitation γ events. This refers to the case 2 above.

3. Considering the flux of atmospheric neutrino, the theoretical expectation of CCQE cross section, and the efficiency of SK detector, including all of those into the caculation to give an expectation of CCQE event number observed in SK according to the live time. Compare the expected number with the de-excitation γ sample made from case 2.

4. By useing the method of searching a γ inside the muon, and the de-excitation γ sample, apply them onto the muon events saved in FC data set and finally give the $Br(\gamma)$ of de-excitation γ in CCQE interaction and estimate the background component refers to the case 1 above.

Details of the first step and second step will be explained in the following sections. It need to be mentioned that our target is the $Br(\gamma)$ of invisible muon, however $Br(\gamma)$ obtained by this way is the one of visible muon. This can be solved by slicing the muon energy into every 50MeV or 100MeV bins. To calculate the $Br(\gamma)$ for each bin, the $Br(\gamma)$ for invisible bin could be estimated by considering proper model.

8.2 Search Method for Branching Ratio of de-excitation gamma

8.2.1 Simulation setup

Simulation is made by SKdetsim, the SK official Monte Carlo, which is introduced in early sections. In SKdetsim neutrino interactions are modeled by NEUT [13] and hadronic interactions are calculated by GCALOR. As explained before, detector dependent parameters as timing resolution, photon acceptance on PMT, water transparency, reflection on PMT and black sheet surface, are input by custom SK code, based on real measurement. The performance of SKDETSIM have been well tested and verified, and the energy scale are determined by electron linear accelerator LINAC from 5MeV to 18MeV [14]. Since our purpose is atmospheric CCQE de-excitation γ, we simply generate a muon from the random position inside SK tank fiducial volume, with a 6MeV γ generated from the same position by the same timing, in order to avoid the dependence of neutrino flux and cross section. We hope to use weak muon near Cherenkov threshold, because our final motivation is to get the $Br(\gamma)$ of inivisible muon. However when the muon is getting close to Cherenkov threshold, the ring angle become small and thus the reconstruction precision become low. So here we take 300MeV/c as a typical value of muon product from CCQE interaction of sub-GeV neutrino, and the γ is generated uniformly to all directions at 6MeV.

8.2.2 Light profile of mu and gamma

The number of Cherenkov photons from a sub-GeV muon can be from a few houndreds to a few tens thousands, while for a 6MeV γ, the number is a few tens. Typically for a 300MeV/c muon, the muon will induce 500 $\sim$ 600 hit PMTs, and a 6MeV γ will induce only $\sim$ 30 hits.

In order to search for the limited γ-induced hits from muon-induced hits, the light profile need to be studied. Considering the photons finally reach PMT surfaces, the origin of the photons can be the following process : Cherenkov photon prodcution, delta rays, scattering in water, reflection on PMT or black sheet surface. A typical simulation event of the pair of 300MeV/c muon and 6MeV γ is shown in Figure below. The hit PMTs are tagged with the source of the photons, while for multi-photon hits, the PMTs are tagged with the earliest photon detected.

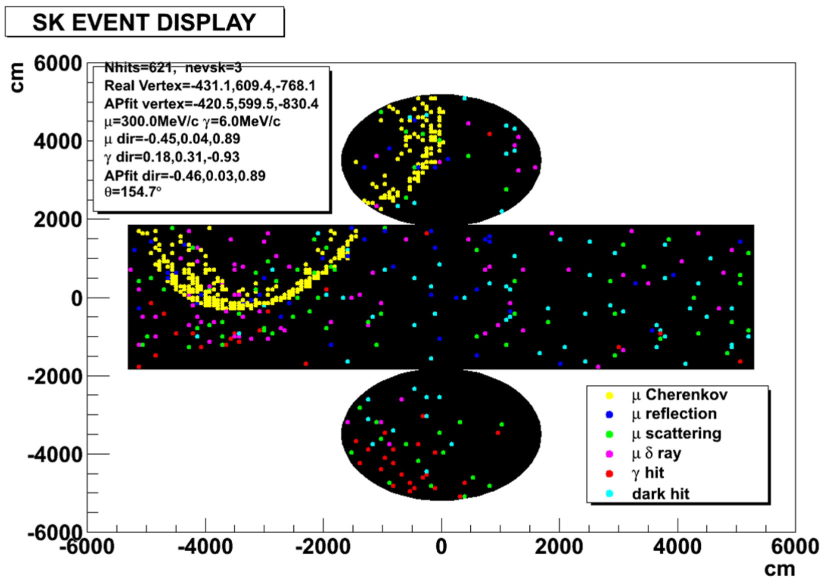

Figure 59: A typical simulation event of the pair of 300MeV/c muon and 6MeV γ. The hit PMTs are tagged with the source of the photons. In this event, the angle between muon and γ is 154.7°.

From the display, the muon-induced Cherenkov photons intend to be a ring and the γ-induced photons intends to be a cluster. As explained in early section, this is because a γ will surfer from Compton scattering and electron/position pair production for several times, the finally detected one is the Cherenkov light of the electrons so the signal consist of several electron rings and intends to be cluster rather than a clean ring.

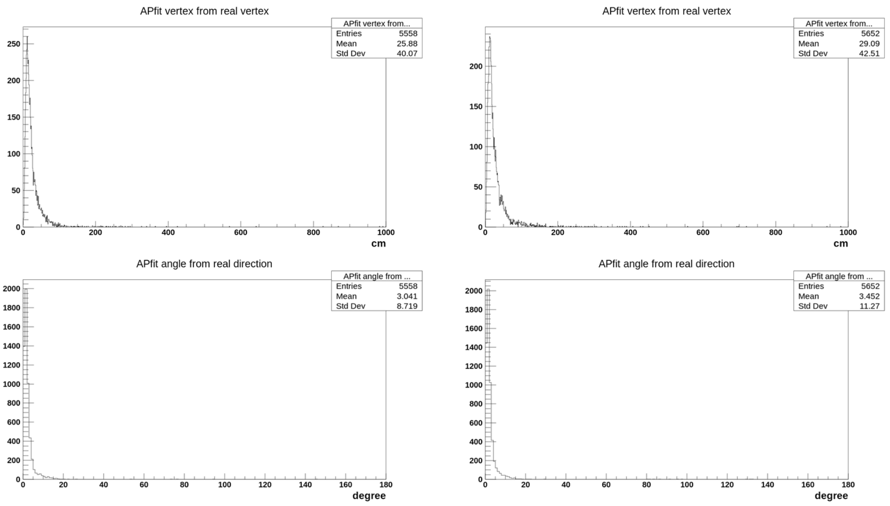

Figure 60: The upper two are the distance from reconstructed vertex to real vertex. The down two are the angle from recontructed direction to real direction. Left two are the simulation of 400MeV/c muon with 6MeV γ generated from the same position. Right two are the simulation of a single 400MeV/c muon. From the comparison of left and right, it can be found that a 6MeV γ from the same position will not affect but will improve the reconstruction precision by a little bit.

Besides, an additional γ will not affect the reconstruction of muon event, both for vertex and direction. On the contrary, more hits from the same position can help to fit the starting point and timing, thus finally improve the reconstruction a little bit.

Supposing the muon direction is already known by reconstruction, a $cos\theta - (T - TOF)$ map as shown in Fig 62, can be used to deeply study the light profile. Here the points on the map means each hit PMT, and $cos\theta$ is the angle between the muon direction and the vector from vertex to corresponding PMT. The vertical axis is the hit timing of each PMT with TOF substracted. Similar to the event display, the hit PMTs are tagged with the the source of the earliest photon.

From the event displayed and the $cos\theta - (T - TOF)$ map, we could see definitely the easiest one to be distingushed is muon-induced Cherenkov photons, without suffering from scattering, reflection or absorption. Hit PMTs from these photons have strong timing and position constraint because the photons generated by muon go directly onto the PMTs in the angle of $0 \sim 50°$. Energy loss of muon in water is $\sim$2MeV/cm, so the Cherenkov angle can decrease to 0 when the sub-GeV muon loss the energy and finally stop in the tank. While for 300MeV/c muon, the Cherenkov angle is still $42°$ and the corresponding hits cluster at $cos\theta = 0.74$.

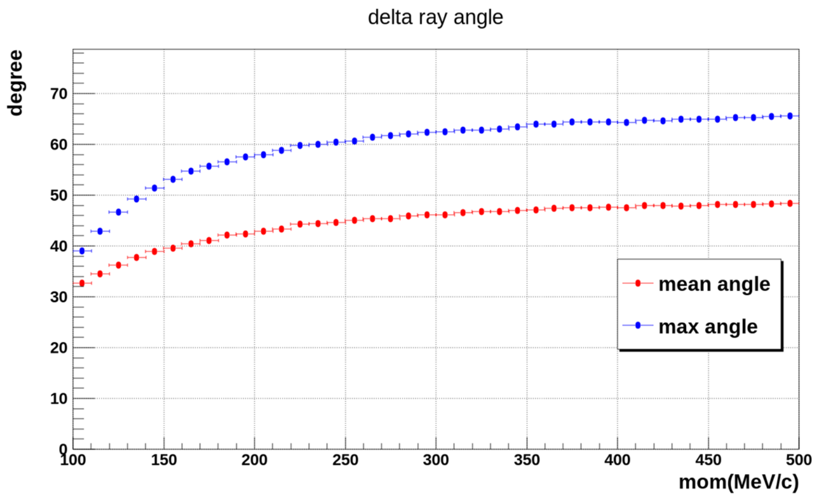

Figure 61: The angle between the direction of δ ray and parrent muon. The horizontal axis is muon momentum. Red and blue dots are the mean value and maximum value for $\delta - muon$ angle respectively.

The delta rays are intrinsically the electrons which obtain energy from muon when it is lossing energy by "ionization" in the water. Those electrons can be a few eV to a few tens MeV, with the angle to the muon track by $40 \sim 65°$, depending on the muon momentum. Most of those electrons are invisible, but a small part of them can be above Cherenkov threshold and give Cherenkov photons. The delta ray photons have a wide angle range and they are the most difficulty in gamma searching. For a sub-GeV muon, the delta ray has a maximum angle of $\sim 60°$ to the muon direction. Since the delta ray gives Cherenkov light, the photons induced by delta ray can go $\sim 102°$ from the muon direction, while a small part of them can even go to the back half by scattering.

The dark hits are not real photons, but be due to the dark noise of PMT electronics. They are randomly distributed in timing and have a frequency of ~3.5kHz, which means for 11129 PMTs in 1.3us gate we could expect a typical number of 51 dark hits.

For the muon-induced photons which are scattered or reflected before detected, they travel for longer distance and thus the hit PMTs will have later responce. From the $cos\theta - (T - TOF)$ map, it can be found that the scattered photons, reflected photons, and dark hits can be removed by a $-10ns + T_0 < T - ToF < +10 + T_0$ cut, while T_0 is the time offset given by software trigger and usually represents the timing of maximum hits in $1.3\mu sec$ window.

A histogram of $cos\theta$ is made below. After $-10ns + T_0 < T - ToF < +10 + T_0$ cut, three main component remain: photon induced by gamma, muon Cherenkov effect, and delta ray. De-excitation gamma goes to random direction so it is uniform in $cos\theta$. Cherenkov photon of muon clusters at $cos\theta \approxeq 0.74$. The most difficult one to remove is delta ray. In order to distingush the muons

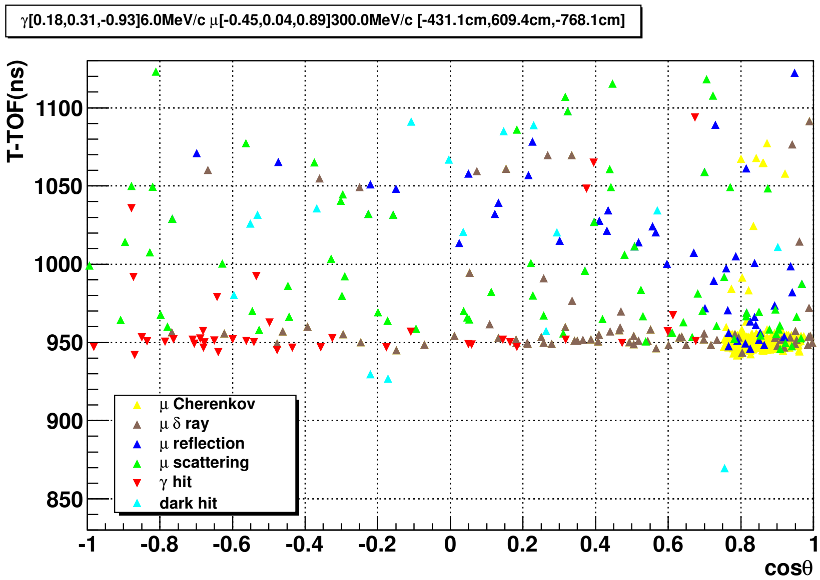

Figure 62: A typical simulation event of the pair of 300MeV/c muon and 6MeV γ. The hit PMTs are tagged with the source of the photons. In this event, the angle between muon and γ is 154.7°.

with 6MeV gamma, a likelihood built on the hit numbers after $-10ns + T_0 < T - ToF < +10 + T_0$ cut will be explained in next section.

In Fig 63, the muon is 300MeV/c. To study further more on sub-GeV muon, the photon component of the pair of a 200-500MeV/c muon and a 6MeV/c gamma is shown in Figure 64.

8.2.3 Building Likelihood

In real data, the muon vertex and direction are supposed to be known, as they can be reconstrued with precise fitter. As explained in previous section, scattering and reflection photons have later timing responce, they can be removed by a simple ±10ns limit on T-ToF. Dark hits are randomly disturbed in time, so they can also be removed by the $-10ns + T_0 < T - ToF < +10 + T_0$ cut. To deal with the remaining three component, gamma hits, delta ray hits and muon Cherenkov hits, we divide the $cos\theta$ into three regions.

- $-1 < cos\theta \leq -0.34$. Delta ray photons largely decrease in this range but a few percent of them still remains. This is the best region to search for a extra gamma.
- $-0.34 < cos\theta \leq 0.6$. Most of the hits in this range are from delta rays. Muon Cherenkov photons can be ignored and 47% gamma photons are in this region.
- $0.6 < cos\theta \leq 1$. In this range, most of the PMT hits are muon Cherenkov photons. Part of the delta ray photons also goes into this region. Since gamma is uniform, 20% gamma photons are in this region.

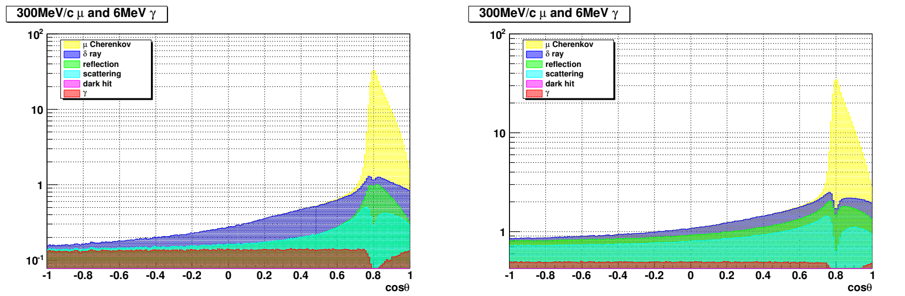

Figure 63: The component of hit PMT numbers for μ events of 300MeV/c. 6MeV γ is generated from the same position to uniform directions. X-axis is $cos\theta$ to μ direction. Left/right figure is before/after $\pm$10ns T-Tof constrain. Cherenkov photons without scattering or reflection will arrive PMT surface without traveling more distance, this is the reason for the dip in $cos\theta = 0.8$ because the PMT hit is tagged by the earliest photon.

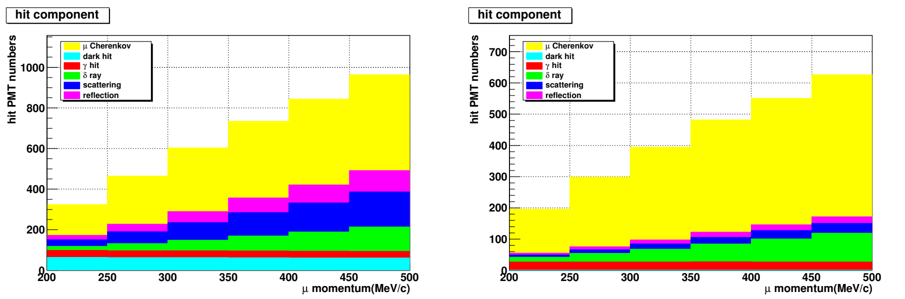

Figure 64: The component of hit PMT numbers for μ events in the momtemum range of 200-500MeV/c. 6MeV γ is generated from the same position to uniform directions. Left/right figure is before/after $\pm$10ns T-Tof hit timing constraint. For the case of multi photon hit, the hit is tagged by the earliest photon.

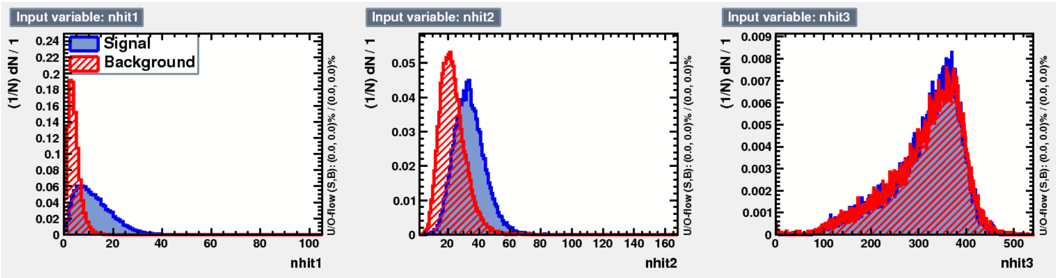

Figure 65: Comparison of PMT hit numbers of random 300MeV/c μ events w/o 6MeV γ. N_{hits1}, N_{hits2}, N_{hits3} are the hit numbers in $-1 < cos\theta \leq -0.34$, $-0.34 < cos\theta \leq 0.6$, $0.6 < cos\theta \leq 1$, divided by the angle between μ and γ respectively.

Figure 65 shows the comparison of the PMT hit numbers in the three regions in case of a 300MeV/c muon with an extra 6MeV gamma(signal) or no gamma(background). To build a likelihood, we can simply multiply the hit numbers in region 1 and 2, and Figure 66 shows the likelihood response. By cutting the likelihood at the maximum significance $Sig = N_s/\sqrt{N_s + N_b}$, we obtain the cut efficiency of gamma case(Eff_s) and no gamma case(Eff_b) of $Eff_s = 13\%$ and $Eff_b = 89\%$.

Defining N_{total} as the total number of stopping muon(including both gamma case and no gamma case) before likelihood cut, and N'_{total} as the total number of muons after likelihood cut, N_{total} and N'_{total} are supposed to be known in analysis of real data. By knowing Eff_s and Eff_b from simulation, the $Br(\gamma) = N_s/(N_s + N_b)$ can be calculated by obtaining N_s and N_b from Equation 70:

$$\begin{cases} N_s + N_b = N_{total} \\ N_s \times Eff_s + N_b \times Eff_b = N'_{total} \end{cases} \tag{70}$$

When applying this simple method onto real data, an expected problem is, the de-excitation gamma can be a mix of 6.18MeV, 6.32MeV, 9.93MeV gamma, and even secondary gamma that the knock-out nucleon hit on another Oxygen nucleus and knock out a nucleon again. This means the likelihood must be modeled for each case. Fortunately, a pure de-excitation gamma sample can be made by coincident search of a gamma and a delayed electron in a typical time difference of 2.2us, which refers to the case 2 in section 8.1 that the muon product from CCQE is invisible.

8.3 Direct measurement of de-excitation gamma in Super-K

As mentioned before, in the real case, the de-excitation γ can be quite complicated then a ideal 6MeV γ that it should be a mix of 6.18MeV, 6.32MeV, 9.93MeV gamma, or even secondary gamma. Therefore, if a de-excitation γ sample can be made from case 2 in section 8.1 by searching for the pair of a prompt γ and a decay electron, then the sample can be useful in the future study of finding the de-excitation γ inside a muon event.

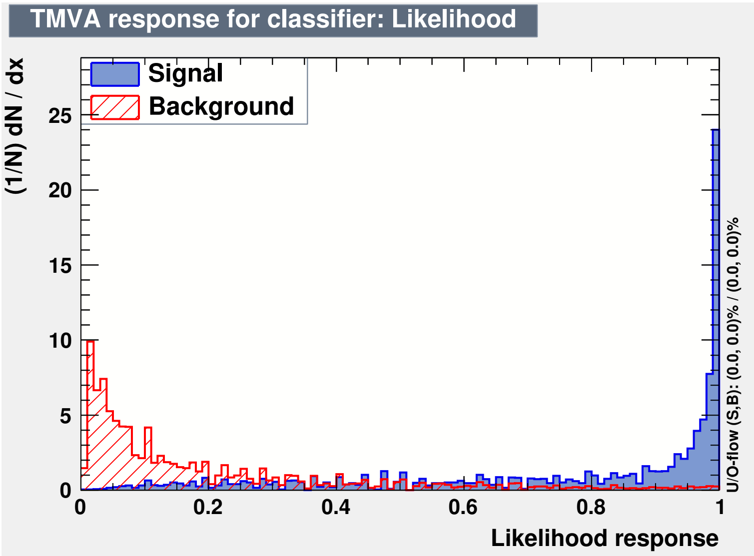

Figure 66: Likelihood built by multiplying N_{hits1} and N_{hits2} in Figure 65. Cut Efficiency for signal(with γ) and background(without γ) is 13% and 89% respectively when cutting at $L = 0.33$ with maximum significance of $Sig = N_s/\sqrt{N_s + N_b}$.

Considering a typical ~6MeV γ ray and the energy resolution, it should be reconstructed in the range of $5 \sim 7MeV$. As mentioned before, though a bit of ~6MeV γ may be tagged as SLE only and thus $-0.5 \sim +1.0\mu sec$ gate is saved instead of $-5 \sim +35\mu sec$ gate, but due to the large amount of low energy background tagged with SLE only(they are mainly the radioactive impurity from the tank structure or surrounding rock in $3 \sim 5MeV$), it is not efficient to search the de-excitation γ by trigger of SLE only.

To start from LE trigger, since the expected energy is in the same range with solar neutrino($4 \sim 20MeV$), the search can be started from the spallation cut step of solar reduction process. The pre reduction and spallation cut are common with solar analysis, which means not only spallation cut but also 22.5kton fiducial volume cut, loose external gamma cut($d_{eff} < 400cm$), loose reconstruction quality cut($g_v^2 - g_d^2 > 0.1$) have been applied. ^{16}N cut is not included because ^{16}N goes beta decay and does not give delay signals.

By requiring a delay signal in $0.5 \sim 35\mu sec$ window after a LE trigger up to 50MeV, the energy and time difference distribution is shown in Fig 68 and Fig 69. As can be seen from energy distribution of delay signal, it shows a good agreement with Michel specturm above 15MeV. However, there are still large amount of low energy background exsiting in delay signal. The most of them are from radioactive impurities which accidently detected in the $35\mu sec$ gate of the prompt LE trigger. Those background form the flat component in time difference distribution. The accidental pair can be efficiently removed by set a contrain on the energy of both prompt and delay signal by $E_{prompt} < 10MeV$ and $E_{delay} > 15MeV$. Though some nuclear reaction in CCQE may give γ ray higher than 10MeV, the dominating one should be $\sim 6MeV$ and hard to

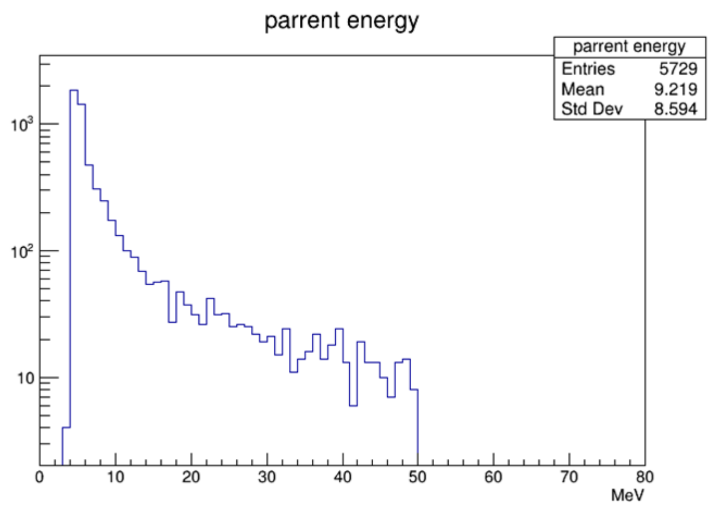

Figure 67: The reconstructed energy of the prompt event.

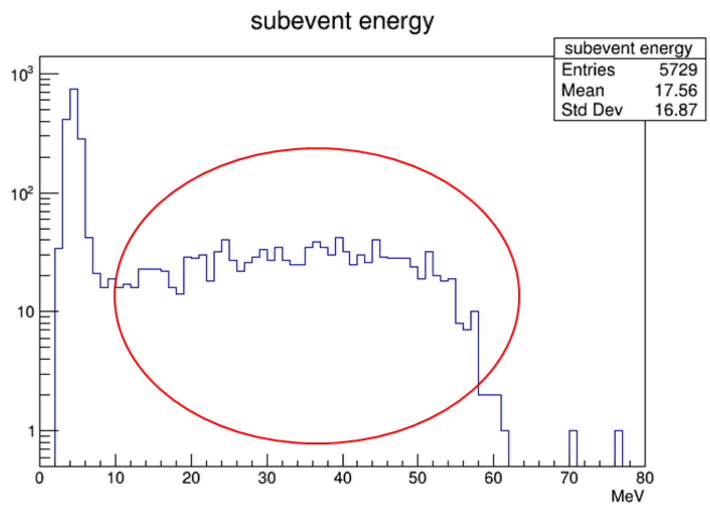

Figure 68: The reconstructed energy of the delay signals. Above 15MeV, it shows a good agreement with Michel spetrum.

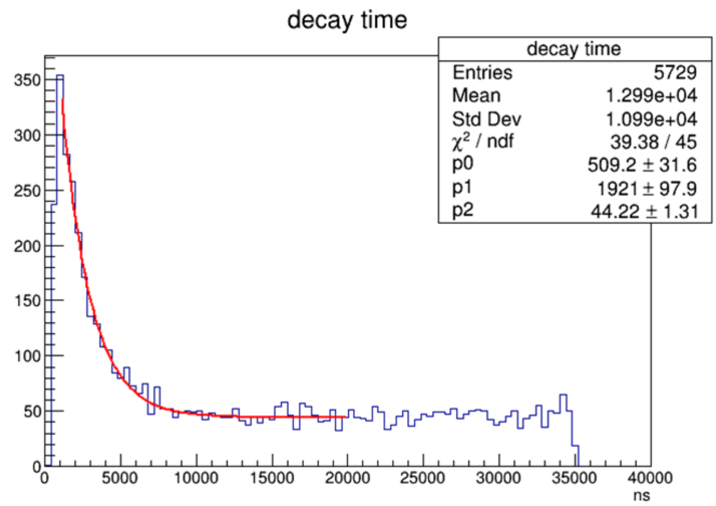

Figure 69: The decay time fit of the pre-selected pairs of a prompt LE trigger and a delay signal. The flat component is due to the accidental backgrounds.

extend above 10MeV. So here both $E_{prompt} < 10MeV$ and $E_{delay} > 15MeV$ are required, and can be seen from the time difference distribution after the cut, the flat componenet has been removed and the decay time fit is $1.7 \pm 1.8\mu sec$. The decay time is less than $2.2\mu sec$, but has a good agreement with the decay time fitted from visible muon sample.

Though the remaining pairs of prompt and decay signal are muons and decay electorns, most of the prompt events are not yet the de-excitation γ we are looking for. This is because when the weak muon whose energy is near Cherenkov threshold, is possible to be reconstructed as an electron or a γ, the weaker it is, more likely this happens. So up to here, though the energy distribution of delay events has good agreement with Michel spectrum and decay time fit is also consistent with visible muon sample, but it is still a problem that the prompt signal may be an invisible muon and a de-excitation γ as we want, but there are also just weak muons near to Cherenkov threshold tagged with LE trigger and mis-reconstructed.

Usually even the muon is close to Cherenkov threshold, they are hard to be recontructed below 10MeV(this is also the reason for $E_{prompt} < 10MeV$ selection). There is another useful to distingush γ ray and weak muon: Cherenkov angle. This is because when the weak muon give Cherenkov light and lose energy in water, it will soon go below the Cherenkov threshold and become invisible. Thus the Cherenkov angle fit of a weak muon will be rather smaller than 42° electron. As mentioned in relic section, for γ ray, the Cherenkov light is from scattered electrons, so it can be considered as multi-rings. While the scattered electrons will suffer from multi-scattering which causes the ring to be more dirty and fuzzy. As a result, the Cherenkov angle of a $\sim 6MeV\gamma$ ray will be larger, usually above 50°.

The Cherenkov angle fit method is the same used in relic section, and the fitted angle for remaining prompt signal is shown below. In relic analysis, the

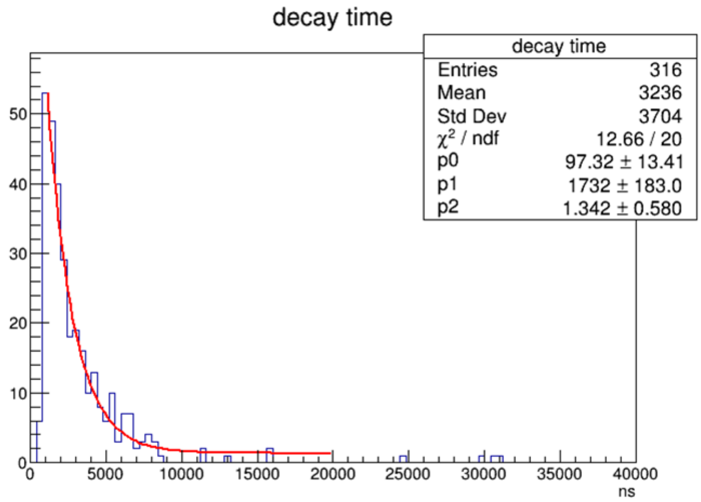

Figure 70: The decay time fit of the remaining events after $E_{prompt} < 10MeV$ and $E_{delay} > 15MeV$ constrain.

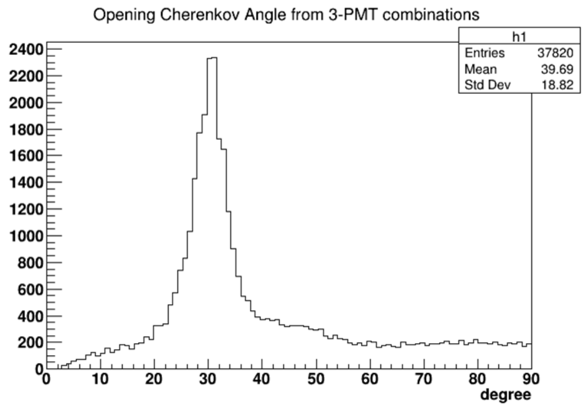

Figure 71: The distribution of opening angles obtained from all 3-hit PMT combination of a $170MeV/c\mu$ event. The peak is around $25°$.

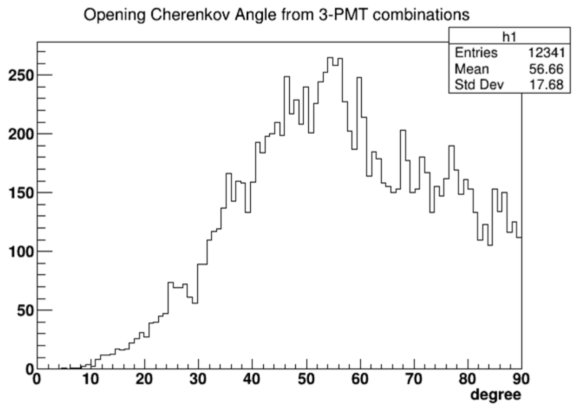

Figure 72: The distribution of opening angles obtained from all 3-hit PMT combination of a typical 6MeV γ event. The peak is above 50°.

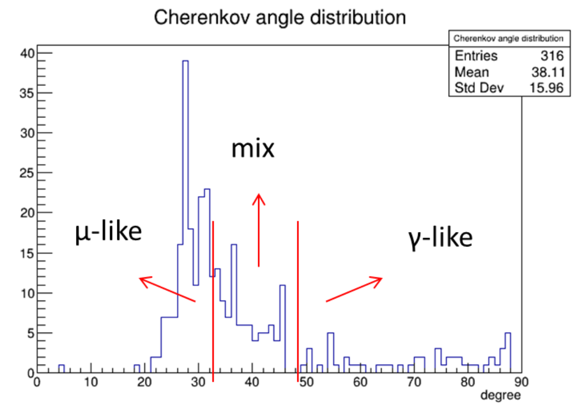

Figure 73: The Cherenkov angle fit result of the remaining events after $E_{prompt} < 10MeV$ and $E_{delay} > 15MeV$ constrain.

electron region is defined as $38^\circ \sim 50^\circ$ and $> 50^\circ$ part is considered to be γ ray. Here we make the same defination that the $< 38^\circ$ part should be weak muons which are close to Cherenkov threshold, $38 \sim 50$ is a mix region of muon and γ, and $> 50^\circ$ is the γ region we are looking for. Finally after $Cherenkovangle > 50^\circ$ cut, for 10 years SKIV data, there are 58 events found for the search of de-excitation γ.

9 Conclusions and Future

9.1 Neutrino search associated with GW170817

This thesis made a coincidence search for neutrino signals with the gravitational wave, GW170817, produced by a binary neutron star merger in NGC4993, in the Super-Kamiokande detector in an energy range from 3.5 MeV to ∼100 PeV. The analysis was performed within a time window of ±500 s of GW170817 and 14 days after the neutron star merger.

In the high-energy data sample, three neutrino interaction categories are considered: FC, PC and UPMU. No neutrino candidate was found in the ±500-s window. The numbers of candidates in a 14-day time window in the entire sky, as well as in a limited spatial region around NGC4993, are consistent with the expectation.

Low-energy neutrino events were also examined using the SRN and the solar neutrino data samples in the same window. No neutrino candidate was found in the SRN and solar neutrino data samples in the ±500-s window. Two candidates were found in the SRN data sample in the 14-day search window, which is consistent with the estimated background rate.

Considering the observation of no significant neutrino signal associated with the GW170817 in SK, we calculated the neutrino fluence limits. The obtained results give the most stringent limits for neutrino emission in the energy region below 100 GeV, especially that the thermal neutrino from binary neutron star merger is expected to be $10 \sim 30$MeV.

The binary neutron star mergers are expected to occur more than once a year [64] at the distance of $\geq 100Mpc$, while a single merger in such distance is difficult to make detectable signal in SK. Comparing to the expected rate of supernova, the rate of binary neutron star merger is two order smaller, and thus "the diffuse neutron star merger neutrino background" will be hidden under the diffuse supernova neutrino background. However, with the precise detection for the timing of gravitational wave, the timing constrain of neutrino searching in $\approx 1s$ from merger time could substantially reduce the contamination from other sources of neutrinos. An idea of how to stack the results of neutrino search from multiple mergers has been suggested in [8].

On the other hand, a next generation underground water Cherenkov detector with 260kton volume has been planned [65], which will bring larger target and higher sensitivity for the neutrino signal from binary neutron star merger.

9.2 De-excitation gamma from atmospheric neutrino CCQE interaction

SK-Gd project can efficiently reduce background and increse $\bar{\nu}_e$ sensitivity for SRN siganl search. However, atomospheric ν_μ CCQE interaction which gives invisible muon and decay electron, still remains as an unreducable component in DSNB spectrum. In order to estimate CCQE background component in observed SRN spectrum, direct measurement for the branching ratio of de-excation gamma is needed. This thesis introduced the method to directly measure the branching ratio of de-excitation gamma based on the CCQE event simulation of SK detector. The direct measurement can not only benefits SRN analysis, but also reduces the uncertainty in long baseline neutrino ossillation experiment.

As the first step, this thesis start from simulation and an analysis method of searching for 6MeV gamma inside a muon event has been introduced.

As the second step, this thesis also reported the current analysis result of CCQE de-excitation gamma with SK-IV data. The result indicates that the de-excitation gamma sample includes the muon events which are close to Cherenkov threshold and tagged as low energy events. However the contamination can be efficiently removed by Cherenkov angle cut and thus a pure sample of CCQE de-excitation gamma could be made. The analysis reported by this thesis is up to here.

For the next step in the future, by using the flux of atmospheric neutrino and the theoritical expectation of CCQE cross section, the expected number of CCQE de-excitation gamma events could be estimated and compared with the current sample.

For the final step of this study, the de-excitation gamma sample could be used for likelihood building and direct searching for de-excitation gamma inside the Fully-Contained muon events of SK real data.

References

[1] B.P.Abbott et al. The Astrophysical Journal Letters, **848**, L13 (2017)

[2] B.P.Abbott et al. Physical Review Letters, **119**, 161101 (2017)

[3] B.P.Abbott et al. The Astrophysical Journal Letters, **848**, L12 (2017)

[4] D.Coulter et al. Science, **358**, 1556 (2017)

[5] A.Albert et al. The Astrophysical Journal Letters, **850**, L35 (2017)

[6] K.Abe et al. The Astrophysical Journal Letters, **830**, L11 (2016)

[7] Y.Sekiguchi et al. Physical Review Letters, **107**, 051102 (2011)

[8] K.Kyutoku and K.Kashiyama, Physical Review D, **97**, 103001 (2018)

[9] K.Abe et al. The Astrophysical Journal, **850**, 166 (2017)

[10] E.Thrane et al. The Astrophysical Journal, **704**, 503 (2009)

[11] M.Swanson et al. The Astrophysical Journal, **652**, 206 (2006)

[12] T.Gaisser et al. Physics Reports, **258**, 173 (1995)

[13] Y.Hayato et al. Acta Physica Polonica B, **B40**, 2477 (2009)

[14] M.Nakahata et al. Nuclear Instruments and Methods in Physics Research Section A: Accelerators, Spectrometers, Detectors and Associated Equipment, **421**, 113 (1999)

[15] A.Ankowski et al. Physical Review Letters, **108**, 052505 (2012)

[16] K.Abe et al. Physical Review D, **90**, 072012 (2014)

[17] M.Leuschner et al. Physical Review C, **49**, 955 (1994)

[18] F.Ajzenberg-Selove et al. Nuclear Physics A, **523**, 1 (1991)

[19] K.Kobayashi et al. ArXiv Nuclear Experiment e-prints, nucl-ex/0604006 (2006)

[20] S.Fukuda et al. Nuclear Instruments and Methods in Physics Research Section A: Accelerators, Spectrometers, Detectors and Associated Equipment, **501**, 418 (2003)

[21] http://sales.hamamatsu.com/assets/pdf/parts R/R3600-06.pdf

[22] K.Kobayashi et al. ArXiv Nuclear Experiment e-prints, nucl-ex/0604006 (2006)

[23] H.Ikeda et al. Nuclear Instruments and Methods in Physics Research Section A: Accelerators, Spectrometers, Detectors and Associated Equipment, **320**, 310 (1992)

[24] T.Tanimori et al. IEEE Transactions on Nuclear Science, **36**, 497 (1989)

[25] T.K.Ohsuka et al. KEK Report 85-10 (1985)

[26] H.Nishino et al. Nuclear Instruments and Methods in Physics Research Section A: Accelerators, Spectrometers, Detectors and Associated Equipment, **610**, 710 (2009)

[27] Y.ZHANG, PhD Thesis, Tsinghua University (2015)
http://www-sk.icrr.u-tokyo.ac.jp/sk/_pdf/articles/2015/thesis_yangzhang_20150615.pdf

[28] S.Yamada et al. IEEE Transactions on Nuclear Science, **57**, 428 (2010)

[29] J.Beacom and M.Vagins, Physical Review Letters, **93**, 171101 (2004)

[30] K.Abe et al. Nuclear Instruments and Methods in Physics Research Section A: Accelerators, Spectrometers, Detectors and Associated Equipment, **737**, 253 (2004)

[31] Y.Koshio, PhD Thesis, University of Tokyo (1998)
http://www-sk.icrr.u-tokyo.ac.jp/sk/_pdf/articles/koshio-dthesis.pdf

[32] Y.Nakano, PhD Thesis, University of Tokyo (2016)
http://www-sk.icrr.u-tokyo.ac.jp/sk/_pdf/articles/2016/doc_thesis_naknao.pdf

[33] M.Ikeda, PhD Thesis, University of Tokyo (2010)
http://www-sk.icrr.u-tokyo.ac.jp/sk/_pdf/articles/ikeda-dron.pdf

[34] T.Yokozawa, PhD Thesis, University of Tokyo (2013)
http://www-sk.icrr.u-tokyo.ac.jp/sk/_pdf/articles/yokozawa thesis.pdf

[35] M.Smy. Proceedings of the 30th 30th International Cosmic Ray Conference, **5**, 1279 (2007)

[36] E.Blaufuss et al., Nuclear Instruments and Methods in Physics Research Section A: Accelerators, Spectrometers, Detectors and Associated Equipment, **458**, 638 (2001)

[37] M.Nakahata et al., Nuclear Instruments and Methods in Physics Research Section A: Accelerators, Spectrometers, Detectors and Associated Equipment, **421**, 113 (1999)

[38] J.Hosaka et al., Physical Review D, **73**, 112001 (2006)

[39] "GEANT - Detector Description and Simulation Tool", CERN Program Library (1993)

[40] B.P.Abbott et al., Physical Review Letters, **116**, 061102 (2016)

[41] B.D.Metzger and E. Berger, The Astrophysical Journal, **746**, 48 (2012)

[42] J.J.Ruan et al., The Astrophysical Journal Letters, **853**, L4 (2018)

[43] K.Hotokezaka et al., Physical Review D, **83**, 124008 (2011)

[44] K.Hirata et al., Physical Review Letters, **58**, 1490 (1987)

[45] S.Richers et al., The Astrophysical Journal, **813**, 38 (2015)

[46] A.Strumia and F.Vissani, Physics Letters B, **564**, 42 (2003)

[47] S.Fujibayashi et al., The Astrophysical Journal, **846**, 114 (2017)

[48] S.Fukuda et al., Physics Letters B, **539**, 179 (2002)

[49] Y.Fukuda et al., Physical Review Letters, **81**, 1562 (1998)

[50] K.Abe et al., Physical Review Letters, **107**, 041801 (2011)

[51] J.N.Bahcall et al., Reviews of Modern Physics, **54**, 767 (1982)

[52] J.N.Bahcall et al., The Astrophysical Journal, **621**, 85 (2005)

[53] R.M.Bionta et al., Physical Review Letters, **58**, 1494 (1987)

[54] E.Cappellaro et al., Astronomy & Astrophysics, **351**, 459 (1999)

[55] G.S.Bisnovatyi-kogan and Z.F.Seidov, Annals of the New York Academy of Sciences, **422**, 319 (1984)

[56] T.Totani and K.Sato, Astroparticle Physics, **3** ,367 (1995)

[57] T.Totani, K.Sato and Y.Yoshii, The Astrophysical Journal, **460**, 303 (1996)

[58] R.A.Malaney, Astroparticle Physics, **7**, 125 (1997)

[59] D.H.Hartmann and S.E.Woosley, Astroparticle Physics, **7**, 137 (1997)

[60] M.Kaplinghat, G.Steigman, and T.P.Walker, Physical Review D, **62**, 043001 (2000)

[61] S.Anto, K.Sato, and T.Totani, Astroparticle Physics, **18**, 307 (2003)

[62] K.Bays et al., Physical Review D, **85**, 052007 (2012)

[63] H.Zhang, PhD Thesis, University of Tsinghua (2012)
http://www-sk.icrr.u-tokyo.ac.jp/sk/_pdf/articles/zhanghb_thesis.pdf

[64] M.Dominik, The Astrophysical Journal, **806**, 263 (2015)

[65] K.Abe et al., arXiv:1109.3262

[66] Y.Ashie, Physical Review D, **71**, 112005 (2005)